Molecular architecture of nucleosome remodeling and deacetylase sub-complexes by integrative structure determination

Shreyas Arvindekar[1], Matthew J. Jackman[2], Jason K.K. Low[3], Michael J. Landsberg[2, *], Joel P. Mackay[3, *], and Shruthi Viswanath[1, *]

[1]National Center for Biological Sciences, Tata Institute of Fundamental Research, Bangalore, India

[2]School of Chemistry and Molecular Biosciences, University of Queensland, QLD, Australia

[3]School of Life and Environmental Sciences, University of Sydney, NSW, Australia

*Corresponding authors E-mail: m.landsberg@uq.edu.au (M.J.L.); joel.mackay@sydney.edu.au (J.P.M.); shruthiv@ncbs.res.in (S.V.)

Short title: Integrative models of NuRD sub-complexes

Abstract

The Nucleosome Remodeling and Deacetylase (NuRD) complex is a chromatin-modifying assembly that regulates gene expression and DNA damage repair. Despite its importance, limited structural information is available on the complex and a detailed understanding of its mechanism is lacking. We investigated the molecular architecture of three NuRD sub-complexes: MTA1-HDAC1-RBBP4 (MHR), MTA1^{N}-HDAC1-MBD3^{GATAD2CC} (MHM), and MTA1-HDAC1-RBBP4-MBD3-GATAD2 (NuDe) using Bayesian integrative structure determination with IMP (Integrative Modeling Platform), drawing on information from SEC-MALLS, DIA-MS, XLMS, negative stain EM, X-ray crystallography, NMR spectroscopy, secondary structure and homology predictions. The structures were corroborated by independent cryo-EM maps, biochemical assays, and known cancer-associated mutations. Our integrative structure of the 2:2:2 MHM complex shows asymmetric binding of MBD3, whereas our structure of the NuDe complex shows MBD3 localized precisely to a single position distant from the MTA1 dimerization interface. Our models suggest a possible mechanism by which asymmetry is introduced in NuRD, and indicate three previously unrecognized subunit interfaces in NuDe: HDAC1^{C}-MTA1^{BAH}, MTA1^{BAH}-MBD3, and HDAC1$^{60-100}$-MBD3. We observed that a significant number of cancer-associated mutations mapped to protein-protein interfaces in NuDe. Our approach also allows us to localize regions of unknown structure, such as HDAC1^{C} and MBD3^{IDR}, thereby resulting in the most complete structural characterization of these NuRD sub-complexes so far.

Introduction

The Nucleosome Remodeling and Deacetylase (NuRD) complex is a multi-protein chromatin-modifying assembly, expressed in most metazoan tissues, and conserved across multi-cellular animals (Basta and Rauchman, 2017; Denslow and Wade, 2007; Lejon et al., 2011; Yoshida et al., 2008). It regulates gene expression and DNA damage repair (Basta and Rauchman, 2017, 2015; Denslow and Wade, 2007; Li and Kumar, 2010; Reynolds et al., 2013; Smeenk et al., 2010; Yoshida et al., 2008). It modulates nucleosome accessibility in enhancers and promoters for transcription factors and RNA polymerases, thereby regulating the expression of target genes (Bornelöv et al., 2018; Burgold et al., 2019). Subunits of NuRD are implicated in human cancers and various congenital defects (Basta and Rauchman, 2015; Toh and Nicolson, 2009). Considerable diversity is observed in subunit isoforms and NuRD-associated factors across tissues (Burgold et al., 2019; Denslow and Wade, 2007; Hoffmann and Spengler, 2019). NuRD comprises two catalytic modules – a histone deacetylase module and ATP-dependent chromatin-remodeling module (Burgold et al., 2019; Denslow and Wade, 2007; Low et al., 2020). The deacetylase module contains metastasis-associated proteins (MTA1/2/3) that form a dimeric scaffold for the histone deacetylases (HDAC1/2). It also contains the chaperones RBBP4/7, which mediate interactions of NuRD with histone tails and transcription factors (Basta and Rauchman, 2017, 2015; Hong et al., 2005). The chromatin-remodeling module contains methyl-CpG DNA binding proteins (MBD2/3) that recruit NuRD to methylated and/or hemi-methylated DNA, GATA-type zinc-finger proteins (GATAD2A/B), and an ATP-dependent DNA translocase (CHD3/4/5) (Burgold et al., 2019; Low et al., 2020).

Some structural information is available for the complex. Several attempts made to determine the stoichiometry of the endogenous NuRD complex have returned variable results (Bode et al., 2016; Guo et al., 2019; Kloet et al., 2015; Sharifi Tabar et al., 2019; Smits et al., 2013; Spruijt et al., 2016; Zhang et al., 2016). A recent characterization by quantitative mass spectrometry from (Low et al., 2020) reported a 2:2:4:1:1:1

(MTA1:HDAC1:RBBP4:MBD3:GATAD2A:CHD4) stoichiometry for the full NuRD complex. Atomic structures of parts of the NuRD complex, including the MTA1-HDAC1 dimer, RBBP4 bound to MTA1, the MBD domain of MBD3, and the coiled-coil dimer of MBD2 and GATAD2A have been determined by X-ray crystallography and NMR spectroscopy (Alqarni et al., 2014; Cramer et al., 2014; Gnanapragasam et al., 2011; Millard et al., 2016, 2013). Structures of the 2:2 MTA1-HDAC1 dimer, the 2:2:4 MTA1-HDAC1-RBBP4 complex (MHR), the 2:2:2 $MTA1^{N}$-HDAC1-$MBD3^{GATAD2CC}$ (MHM) complex, the 2:2:4:1:1 MTA1-HDAC1-RBBP4-MBD3-GATAD2 (NuDe complex), and CHD4 bound to a nucleosome substrate have also been characterized at various resolutions by negative stain and/or cryo-electron microscopy (Farnung et al., 2020; Low et al., 2020; Millard et al., 2020, 2016).

Pairwise interactions between domains and subunits within the MHR, MHM, NuDe, and the endogenous NuRD complexes have also been characterized by chemical crosslinking and mass spectrometry (XLMS) (Low et al., 2020; Millard et al., 2016). A model of the MHM complex, based on crosslinks-driven rigid-body docking of known atomic structures with a pair of MTA1-RBBP4 structures manually placed, has also been reported (Low et al., 2020). While this represents the most complete model of NuRD architecture, it still only accounts for 30% of residues in the NuRD complex. In fact, only 50% of residues in NuRD have known or readily modeled atomic structures, and the structures of proteins such as MBD3, CHD4, and GATAD2 are largely uncharacterized. More recent artificial intelligence-based methods such as AlphaFold are also unable to resolve these uncharacterized regions (Jumper et al., 2021). Owing to variability in the paralogue composition as well as significant structural dynamics, the atomic structure of the entire NuRD complex is still undetermined and is likely to remain a challenge for some time to come.

The 2:2:4 MTA1-HDAC1-RBBP4 complex (MHR) forms the deacetylase core of NuRD. MBD3 binds to the N-terminal half of MTA1 to form a 2:2:2 $MTA1^{N}$-HDAC1-$MBD3^{GATAD2CC}$ (MHM) complex, which contains two copies of MBD3 (Low et al., 2020). However, the 2:2:4:1:1 MTA1-HDAC1-RBBP4-$MBD3^{-}$GATAD2 (NuDe complex) and the endogenous NuRD complex are asymmetric, both containing a single copy of MBD3 (Low et al., 2020). The mechanism by which this asymmetry is introduced in NuDe/NuRD is not known. The structure of full-length MBD3 is unknown and it contains a significant intrinsically disordered region (IDR; $MBD3^{71-213}$), which has been shown to be critical for recruiting the deacetylase core in case of MBD2 (Desai et al., 2015). The localization of full-length MBD3 in NuDe/NuRD is also not known.

Here, we investigated the molecular architecture of the MHR, MHM, and NuDe complexes using an integrative approach. Integrative structure determination is a method for investigating structures of large assemblies which are refractory to a single experimental method such as X-ray crystallography or cryo-electron microscopy (Alber et al., 2007; Ganesan et al., 2020; Gutierrez et al., 2020; Kim et al., 2018; Rout and Sali, 2019; Russel et al., 2012; Viswanath et al., 2017a; Ward et al., 2013). Using Bayesian integrative modeling with the Integrative Modeling Platform (IMP), we combined data from complementary experiments, physical principles, statistical inference, and prior models. This approach allowed us to combine noisy, sparse, ambiguous, and incoherent data at various resolutions (Alber et al., 2007; Rieping et

al., 2005; Rout and Sali, 2019; Schneidman-Duhovny et al., 2014). It produced an ensemble of models consistent with the input information, allowing us to obtain precise uncertainty bounds on the structure (Saltzberg et al., 2019, 2021; Viswanath et al., 2017b; Webb et al., 2018). We used data from SEC-MALLS, DIA-MS, XLMS, negative stain EM, X-ray crystallography, NMR spectroscopy, secondary structure and homology predictions, and stereochemistry considerations (Alqarni et al., 2014; Connelly et al., 2006; Cramer et al., 2014; Gnanapragasam et al., 2011; Low et al., 2020; Millard et al., 2016, 2013). These integrative structures were corroborated by independent cryo-EM maps, biochemical assays, and known cancer-associated mutations, a significant number of which mapped to protein-protein interfaces in the structures (Desai et al., 2015; Forbes et al., 2006; Millard et al., 2020; Pflum et al., 2001; Zhang et al., 1999). By using all available information, the accuracy, precision, completeness, and efficiency of structure determination was maximized (Alber et al., 2007; Rout and Sali, 2019; Russel et al., 2012).

Results

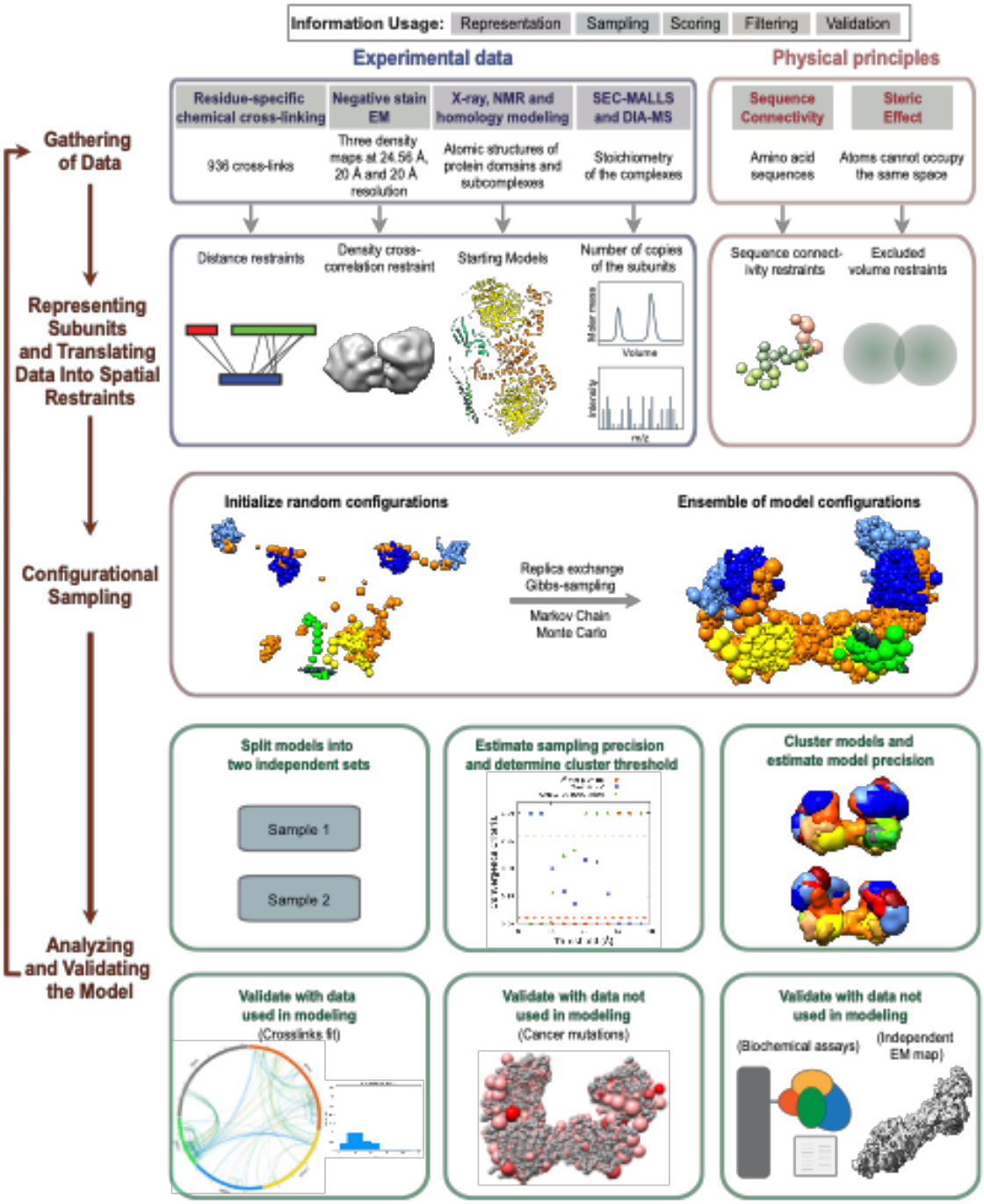

Fig. 1 Integrative structure determination of NuRD sub-complexes Schematic describing the workflow for integrative structure determination of NuRD sub-complexes. The first row describes the input information. The second-row details how data is used to encode spatial restraints. The third row mentions the sampling method and the last two rows illustrate the analysis and validation protocol. The background colors of the input information indicate the stage of modeling in which the information is used, as shown in the legend at the top.

Integrative modeling workflow

The integrative modeling of the MHR, MHM, and NuDe complexes proceeded in four stages (Fig. 1, Material and Methods) (Alber et al., 2007; Rout and Sali, 2019; Russel et al., 2012). The modeled NuRD proteins (subunits), their domains, their representation, and the number of copies in the modeled complexes are shown (Fig. S1A-S1C). The stoichiometry of the modeled proteins was informed by DIA-MS and SEC-MALLS experiments (Fig. S1C) (Low et al., 2020).

Regarding paralogs, a single representative for each protein was chosen for this work for simplicity, namely MTA1, HDAC1, RBBP4, MBD3 and GATAD2A (Fig. S1A).

We first represented each protein as a series of beads of size that depends on the degree of knowledge of the structure (and can vary throughout the sequence). Protein domains with known atomic structures (such as the MTA1-HDAC1 dimer) were represented at 1 and 10 residues per bead and modeled as rigid bodies, whereas domains without known structure (such as the $MBD3^{IDR}$) were coarse-grained at 30 residues per bead and modeled as flexible strings of beads (Fig. S1A-S1B). Data from chemical crosslinking combined with mass spectrometry (XL-MS) were used to restrain the distance between cross-linked residues. Negative-stain EM maps were used to restrain the shape of the complexes (Low et al., 2020).

The simulations started with randomized configurations for the rigid bodies and flexible beads. Over 40 million models per complex were sampled using a Monte Carlo approach (Replica Exchange Gibbs Sampling MCMC; Materials and Methods). The models were scored based on agreement with XL-MS and EM data, together with additional stereochemistry restraints such as connectivity and excluded volume. For each complex, about 20,000 models that sufficiently satisfied the input information were selected for further analysis (Saltzberg et al., 2021).

These models were clustered based on structural similarity and the precision of the clusters was estimated (Fig. S3-S5) (Saltzberg et al., 2019, 2021; Viswanath et al., 2017b). The quality of the models was assessed by fit to input data (Fig. S6-S8), as well as data not used in modeling, such as independent cryo-EM maps (Millard et al., 2020), published biochemical data (Desai et al., 2015; Millard et al., 2020; Pflum et al., 2001; Zhang et al., 1999) and human cancer-associated mutations (COSMIC) (Table S1) (Forbes et al., 2006). The resulting integrative models were visualized in two ways - a representative bead model and a localization probability density map, and represented in UCSF Chimera and ChimeraX (Pettersen et al., 2021, 2004). The bead model represents the centroid of the major cluster, whereas the localization probability density map represents all models in the major cluster, by specifying the probability of a voxel (3D volume unit) being occupied by a bead in the set of superposed cluster models.

MHR

First, to support the integrative modeling of the MHR complex, an *ab initio* 3D EM map for the MHR complex was produced by further analysis of the MHR 2D class averages reported in a previous study (Low et al., 2020). Integrative modeling of the 2:2:4 MHR complex produced effectively a single cluster of models (85% of a total of 15200 models) with a model precision of 27 Å; model precision is the average RMSD between the cluster centroid and models in the cluster (Fig. S3). The models fit very well to the input data as measured by the EM and crosslink scores. 98% of the input crosslinks were satisfied within their uncertainty (Fig. S6). An adipic acid dihydrazide (ADH) / bis(sulfosuccinimidyl)suberate - disuccinimidyl suberate (BS3DSS) / dimethoxy triazinyl methyl-morpholinium chloride (DMTMM) crosslink is violated if the corresponding cross-linked beads are greater than 35 / 35 / 25 Å apart in all models in the cluster. The cross-correlation between the localization probability density map for the models in the major cluster and the input EM map was 0.74, indicating the fit to EM is reasonable but not too high. This could partly be due to unoccupied density in the lobes of the experimental EM map.

Surprisingly, the representative bead model from the dominant cluster (cluster centroid model) shows the C-terminal half of the two MTA subunits ($MTA1^{432-715}$) crossing over (brown and orange MTAs, Fig. 2A, Movie M1). Integrative models of the MHR complex created in the absence of the EM map also showed the MTAs crossing over (Fig. S9).

The $MTA1^{BAH}$ domain ($MTA1^{1-164}$) is positioned distal to the MTA1 dimerization interface ($MTA1^{200-290}$, $MTA1^{dimer}$), consistent with its position in an independent EM map (Fig. 2B, Fig. 2C) (Millard et al., 2020). It is proximal to the HDAC1 active site and may potentially regulate HDAC1 activity (Fig. 2A). This conclusion is consistent with histone deacetylation assays in which MTA1 was shown to modulate HDAC1 deacetylase activity in NuRD (Zhang et al., 1999). Further, for one of the MTAs, the $MTA1^{BAH}$ is located near an RBBP4 (Fig. 2A, Fig. 2B); $MTA1^{BAH}$ proximity to RBBP4 was also indicated in an independent cryo-EM map (Millard et al., 2020). Finally, $MTA1^{BAH}$ is also proximal to the $MTA1^{mid}$ region ($MTA1^{334-431}$) containing the predicted helix (H) and zinc finger regions (ZF) (Fig. 2B, Fig. 2C).

The $MTA1^{mid}$ region is juxtaposed between $MTA1^{dimer}$ and the $MTA1^{BAH}$ domain (Fig. 2B). In contrast, in a previous crosslink-based MHR model (Low et al., 2020), $MTA1^{mid}$ was proximal to the $MTA1^{BAH}$ domain and distal from the $MTA1^{dimer}$. The MTA1 C-terminus ($MTA1^{C}$; *i.e.*, $MTA1^{692-715}$) shows considerable conformational heterogeneity and is co-located with $MTA1^{USR}$ ($MTA1^{547-669}$), the MTA1 disordered region between the R1 and R2 RBBP4 binding regions (Fig. 2B, Movie M1). Overall, many MTA1 domains in the MHR model, such as $MTA1^{BAH}$ domain, $MTA1^{mid}$, and $MTA1^{C}$, are exposed and could possibly interact with nucleosomal DNA and/or other proteins.

The HDAC1 C-terminus ($HDAC1^{C}$; *i.e.*, $HDAC1^{377-482}$) interacts with the $MTA1^{BAH}$ domain (Fig. 2B). Although it has been shown that the MTA1-HDAC1 dimer can form in the absence of $MTA1^{BAH}$ (Millard et al., 2013), this additional interaction between MTA1 and HDAC1 could be functionally important. Consistent with this possibility, mutations in $HDAC1^{C}$ (Δ391-482, S421A, S423A, E426A) have been known to disrupt binding to NuRD subunits (Pflum et al., 2001). There are also post-translational modifications in the HDAC1 tail that might modulate its interaction with MTA1 (Pflum et al., 2001; Rathert et al., 2008).

Both the $MTA1^{R1}$-RBBP4 units are located between the two lobes in the EM map, with one complex in the front and the other at the back (dark blue beads and densities, Fig. 2A-2C). On the other hand, the $MTA1^{R2}$-RBBP4 complexes are located in separate lobes (light blue beads and densities, Fig. 2A-2C). The densities of RBBP4 are spread out, indicating its localization in MHR is imprecise (Fig. 2B, Movie M1). This is consistent with the structural heterogeneity observed in 2D class averages of the MHR EM data (Low et al., 2020). This flexibility could facilitate RBBP4 interactions with transcription factors and histones.

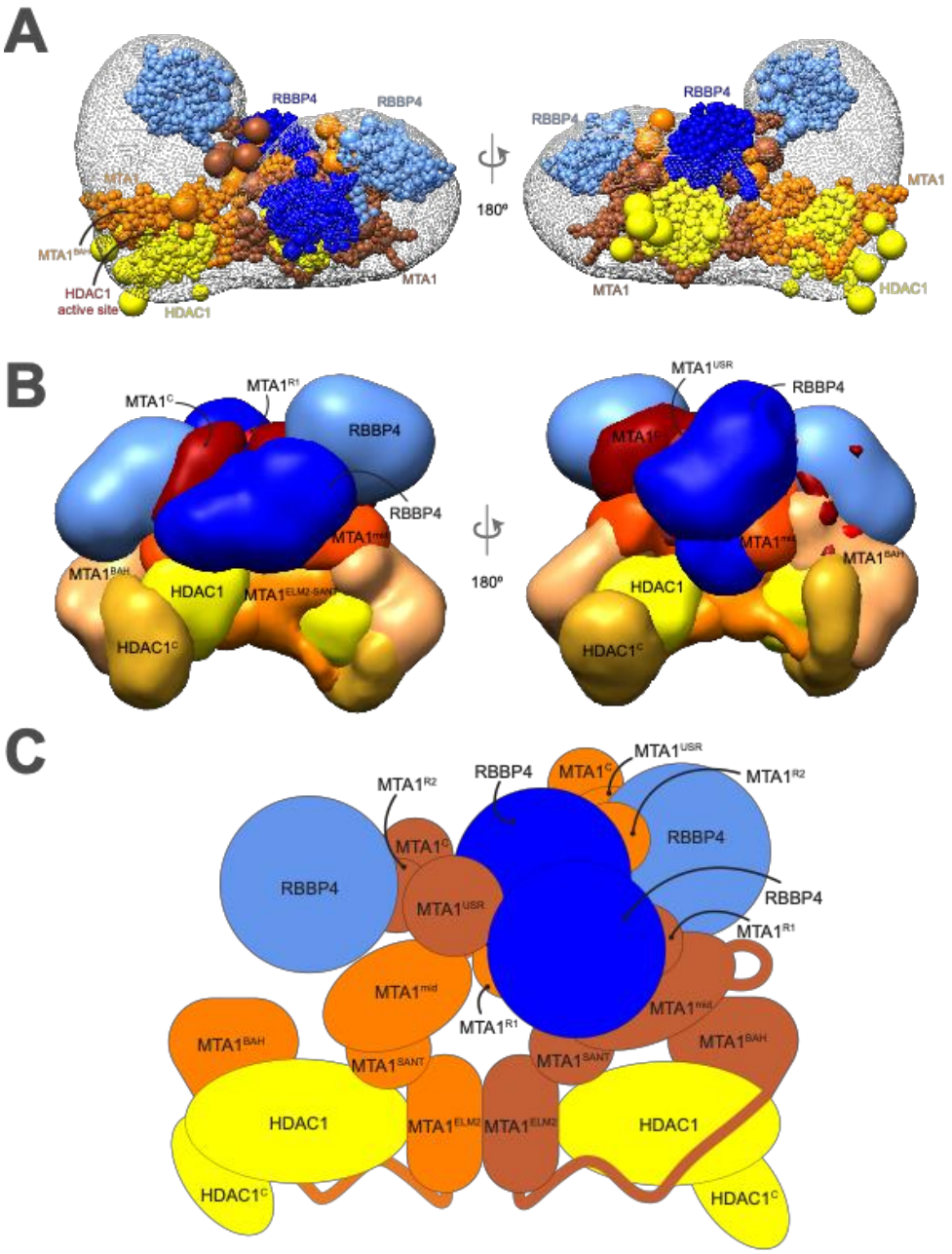

Fig. 2 Integrative model of the MTA1-HDAC1-RBBP4 (MHR) complex A. Representative bead model from the most populated cluster of integrative models for the MHR complex, shown with the MHR EM map. The model is colored by subunit. For MTA1, the two copies are shown in different colors (brown and orange) in panels A and C, to illustrate the crossover. The HDAC1 active site is shown in red. B. Localization probability density maps showing the position of different domains/subunits in the cluster. The map specifies the probability of any volume element being occupied by a domain in the ensemble of superposed models from the cluster. The domain densities are colored according to Fig S1. These maps are contoured at ~10% of their respective maximum voxel values. C. Schematic representation of the integrative model of the MHR complex. See also Figs. S1, S3, S6, and Movie M1.

MHM

Integrative modeling of the 2:2:2 MHM complex resulted in a major cluster containing 60% of 21960 models. The model precision was 24 Å and 99% of the input crosslinks were satisfied (Fig. S4, Fig. S7). The cross-correlation between the localization probability density map for the models in the major cluster and the input EM map was 0.90.

First, in a control run, where MHM was modeled as a 2:2:1 complex with a single copy of MBD3, we observed two symmetric MBD3 binding sites (Fig. S10). However, our 2:2:2 MHM model shows that the two copies of MBD3 bind asymmetrically on the MTA1-HDAC1 dimer (Fig. 3A-3C, Movie M2). One MBD3 localizes exclusively to one end of the MTA1-HDAC1 dimer, making contacts predominantly with a single MTA1 and HDAC1 (pink MBD3, Fig. 3C), whereas the other MBD3 is more spread out and interacts with both copies of MTA1 and HDAC1 (green MBD3, Fig. 3C).

In our models, both the copies of $MBD3^{MBD}$ localize close to the $MTA1^{BAH}$ domain, which is similar to the location observed for $MBD2^{MBD}$ in an independent cryo-EM map of a 2:2:1 MTA1:HDAC1:MBD2 complex (Fig. 3A-3C) (Millard et al., 2020). Although there are two MBD3s in our models, only a single $MBD3^{IDR}$ localizes to the MTA1 dimerization interface, $MTA1^{dimer}$ (green MBD3, Fig. 3D-3E). This localization of $MBD3^{IDR}$ is consistent with its previously predicted localization from the crosslinks-based model (Low et al., 2020) and the localization of $MBD2^{IDR}$ based on cryo-electron microscopy (Millard et al., 2020). It is also supported by two separate mutagenesis and co-immunoprecipitation studies, one of which showed that $MBD2^{IDR}$ was essential for binding to the MTA1-HDAC1 dimer (Desai et al., 2015), while the other showed that $MTA1^{dimer}$ was essential for its interaction with MBD2 (Millard et al., 2020). It is known that MBD3 binding in NuDe/NuRD is asymmetric; although there are two symmetric MBD3 binding sites, there is a single MBD3 in these complexes (Low et al., 2020). It is possible that a single MBD3 is present in NuDe/NuRD since a single $MBD3^{IDR}$ can bind to the $MTA1^{dimer}$ (see also Discussion).

For both MBDs, the $MBD3^{MBD}$ domain is proximal to the $MTA1^{BAH}$ domain and the $MBD3^{IDR}$ is close to the $MTA1^{mid}$ region (Fig. 3B, Fig. 3E). The $MBD3^{CC}$-$GATAD2^{CC}$ coiled-coil domain is exposed. Finally, in a small minority of models, both MBDs are localized together on the same side of the $MTA1^{dimer}$; however, we believe this latter configuration is possibly due to a large number of intra-MBD3 crosslinks (Movie M2).

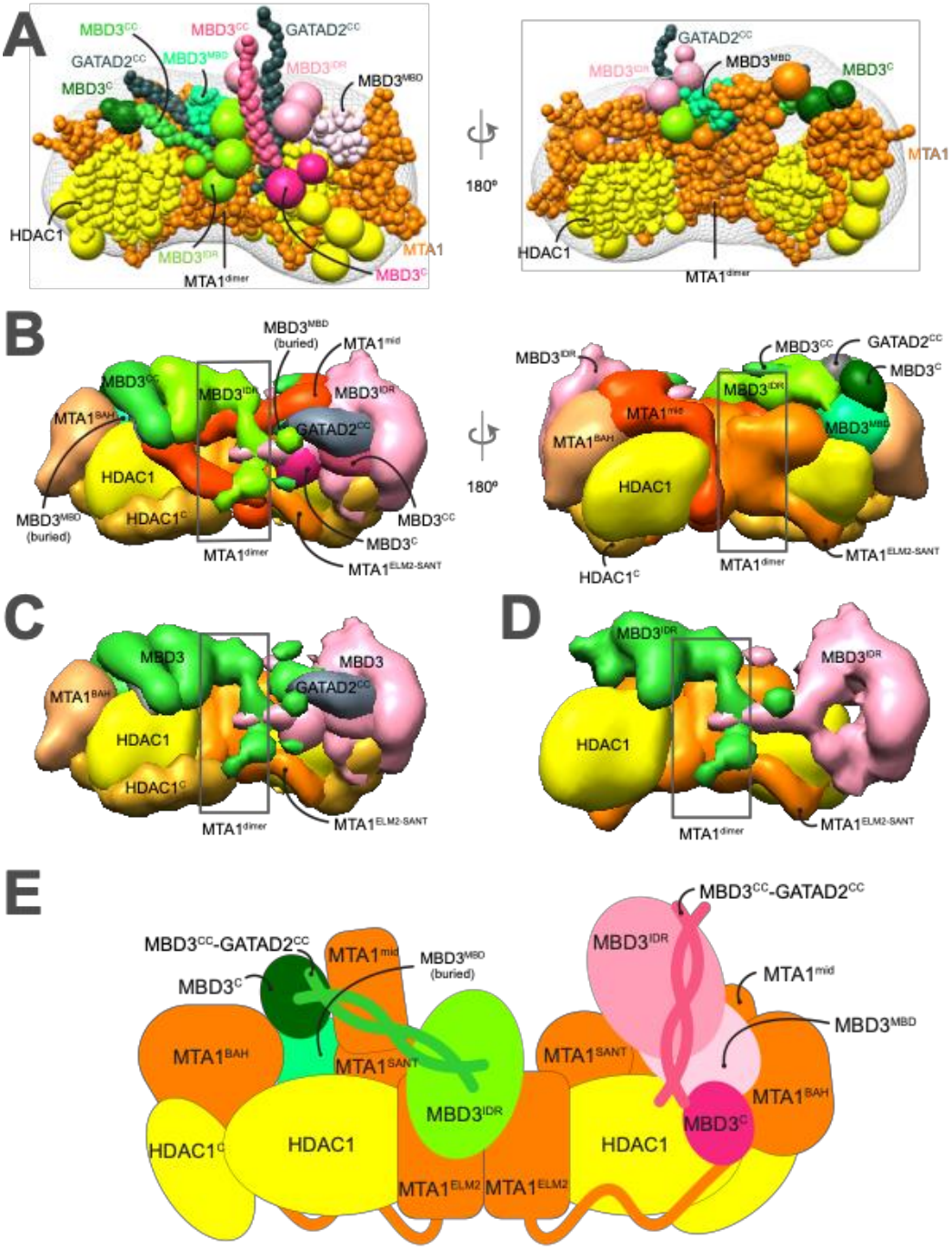

Fig. 3 Integrative model of the MTA1^{N}-HDAC1-MBD3^{GATAD2CC} (MHM) complex A. Representative bead model from the major cluster of analyzed integrative models for the MHM complex, with the corresponding EM map (EMD-21382) (Low et al., 2020), colored by subunit. The domains of the two MBD3s are shown in shades of pink and green respectively. B. Localization probability density maps showing the position of different domains in the ensemble of models from the cluster. The domain densities are colored according to Fig S1. C. The same density maps as B (front view), showing the two MBDs in pink and green respectively, illustrating that they localize differently on the MTA1-HDAC1 dimer. The density maps of MTA1^{mid} and GATAD2^{cc} were omitted for clarity. D. The density maps of the two MBD3^{IDR} domains on the MTA1-HDAC1 dimer. Almost all the maps are contoured at 20% of their respective maximum voxel values (GATAD2 maps are contoured at 27% whereas MBD3^{IDR} maps are contoured at 10%). E. Schematic representation of the integrative model of the MHM complex. Note that MTA1^{mid} in this model corresponds to MTA1$^{334-431}$. See also Figs. S1, S4, S7, and Movie M2.

NuDe

Although the NuDe complex contains full-length GATAD2, due to the lack of information on full-length GATAD2, we modeled only the GATAD2 region that forms a coiled-coil with MBD3. Integrative modeling of the NuDe complex resulted in effectively a single cluster (99% of 21632 models). The model precision was 35 Å and 99% of the input crosslinks were satisfied (Fig. S5, Fig. S8). The cross-correlation between the localization probability density map for the models in the major cluster and the input EM map was 0.88.

In contrast to our MHM model where one MBD3 was proximal to the MTA1^{SANT} domain, MBD3 in NuDe localizes precisely to one end of the MTA1-HDAC1 dimer, away from the MTA1^{SANT} domain. It is juxtaposed next to the MTA1^{BAH} and MTA1^{mid} domains, as well as HDAC1 (Fig. 4A-4C, Movie M3). An independent cryo-EM map of MTA1$^{1-546}$-HDAC1-MBD2-RBBP4 also showed that MBD3 was proximal to MTA1^{BAH} and MTA1^{dimer} (Millard et al., 2020). It is possible that the presence of GATAD2 sterically precludes MBD3 from occupying the MTA1 dimerization interface (see also Discussion).

From protein-protein distance maps of the cluster, HDAC1$^{60-100}$ and MTA1^{BAH} are most proximal to MBD3 (Fig. S11A, S11B). MBD3^{CC}-GATAD2^{CC} is exposed. The MBD3^{MBD} domain is buried, consistent with the failure of MBD3 to bind DNA in NuRD noted in immuno-precipitation experiments (Fig. 4A-4C) (Zhang et al., 1999). Interestingly, several nucleosome-interacting domains such as MTA1^{BAH} and MTA1^{ZF} are co-localized in the NuDe model (Fig. 4A-4C).

Similar to the MHR models, the HDAC1^{C} domain is proximal to MTA1^{BAH} (Fig. S11C). Mutagenesis and co-immunoprecipitation studies have shown that HDAC1^{C} makes critical interactions with NuRD subunits (Pflum et al., 2001). In contrast to the MHR models which showed crossover of MTAs, the two MTAs are well-separated in NuDe (Fig. 4A-4C). The localization of RBBPs is also more precise in NuDe than in MHR (Fig. S12).

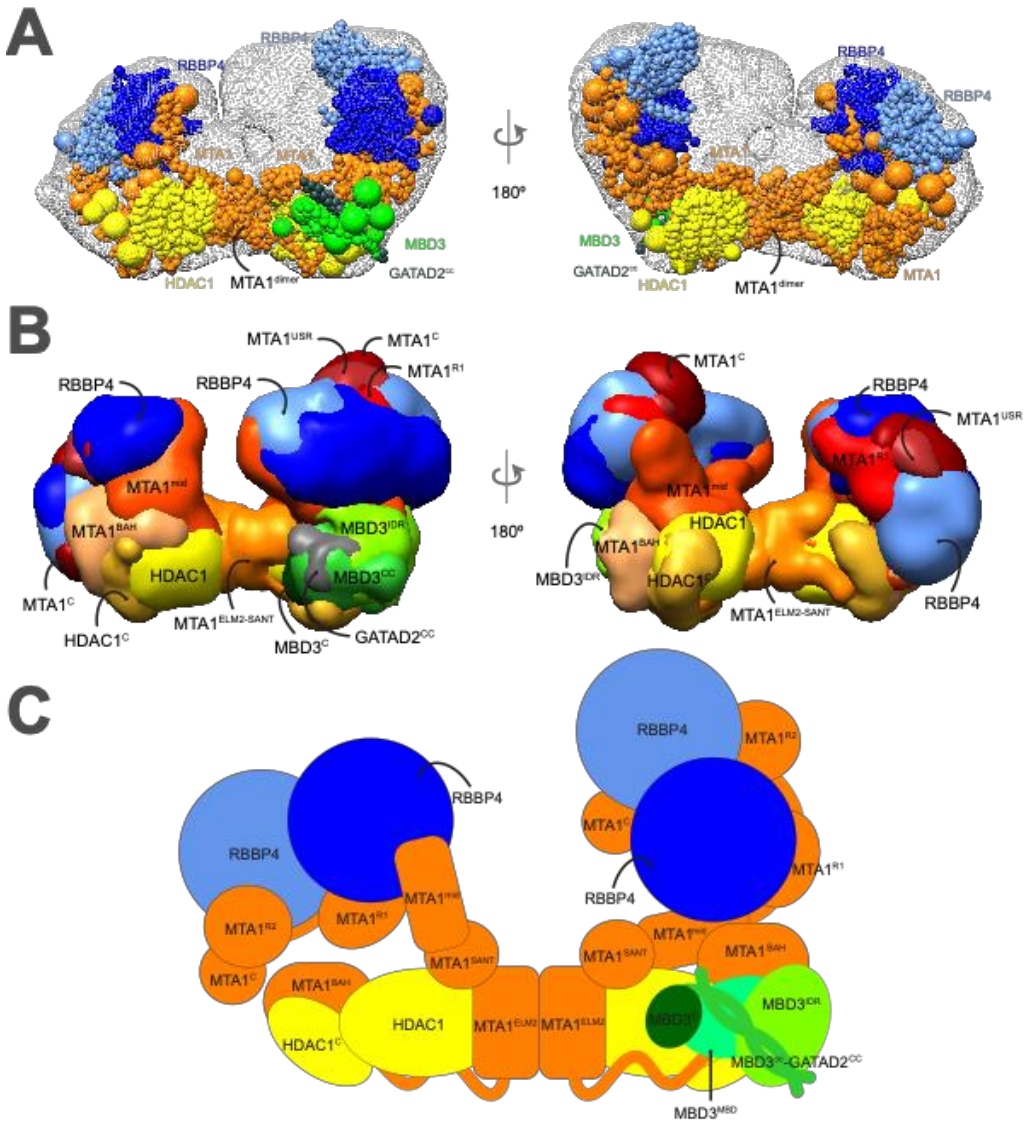

Fig. 4 Integrative model of the nucleosome deacetylase (NuDe) complex A. Representative bead model from the dominant cluster of integrative models for the NuDe complex, with the corresponding EM map (EMD-22904) (Low et al., 2020), colored by subunit. B. Localization probability density maps showing the position of different domains in the ensemble of models from the cluster. The domain densities are colored according to Fig S1. Maps are contoured at ~10% of their respective maximum voxel values. C. Schematic representation of the integrative model of the NuDe complex. See also Figs. S1, S5, S8, S11, and Movie M3.

Mapping COSMIC mutations

We next consulted the COSMIC (Catalogue of Somatic Mutations in Cancer) database for somatic, confirmed pathogenic, point mutations of the NuRD subunits, MTA1, HDAC1, RBBP4, and MBD3 (Forbes et al., 2006). In total, 356 point mutations were identified and mapped onto the cluster of NuDe integrative models (Methods, 4.5 COSMIC data analysis). Analysis of these mutations revealed that 74% of mutations mapped to protein-protein interfaces within NuDe; for the purpose of this analysis, a mutation was considered to be at an interface if the average distance of the corresponding residue to a residue in an interacting protein is less than 10 Å. 29% of the mapped mutations were located in previously uncharacterized binding interfaces predicted by our model, such as MBD3-MTA1^{BAH}, MBD3-HDAC1$^{60-100}$, and HDAC1^{C}-MTA1^{BAH}, consistent with the idea that these interfaces are important for NuRD function (Fig. 5, Fig. S13,

Table S1). Mutations at protein-protein interfaces could alter protein-protein interactions, reducing the stability of the complex, thereby leading to pathogenicity. Moreover, 19% of all mutations mapped to exposed regions that are known to bind to nucleosomes and transcription factors, such as the HDAC1 active site and RBBP4 H3 interaction site (Fig. 5, Fig. S13, Table S1). These mutations could impair NuRD binding to partners such as nucleosomes or transcription factors, contributing to the pathogenesis of disease. Of the 19% that map to exposed regions, more than half (57%) of the mutations map to regions of unknown structure (regions for which no experimental structure or reliable model is available), such as MTA1^{USR} and MBD3^{IDR} (Fig. 5, Table S1). The functional significance of these mutations is therefore difficult to predict, but could indicate that these regions of unknown structure also have important roles in protein stability, regulating interactions between NuRD subunits, or interactions with binding partners of NuRD. An important consideration for all these disease-causing mutations is that many of the NuRD subunits function in cellular contexts independent of other NuRD subunits, and so in some cases these mutations may be rationalised in the context of other functional roles.

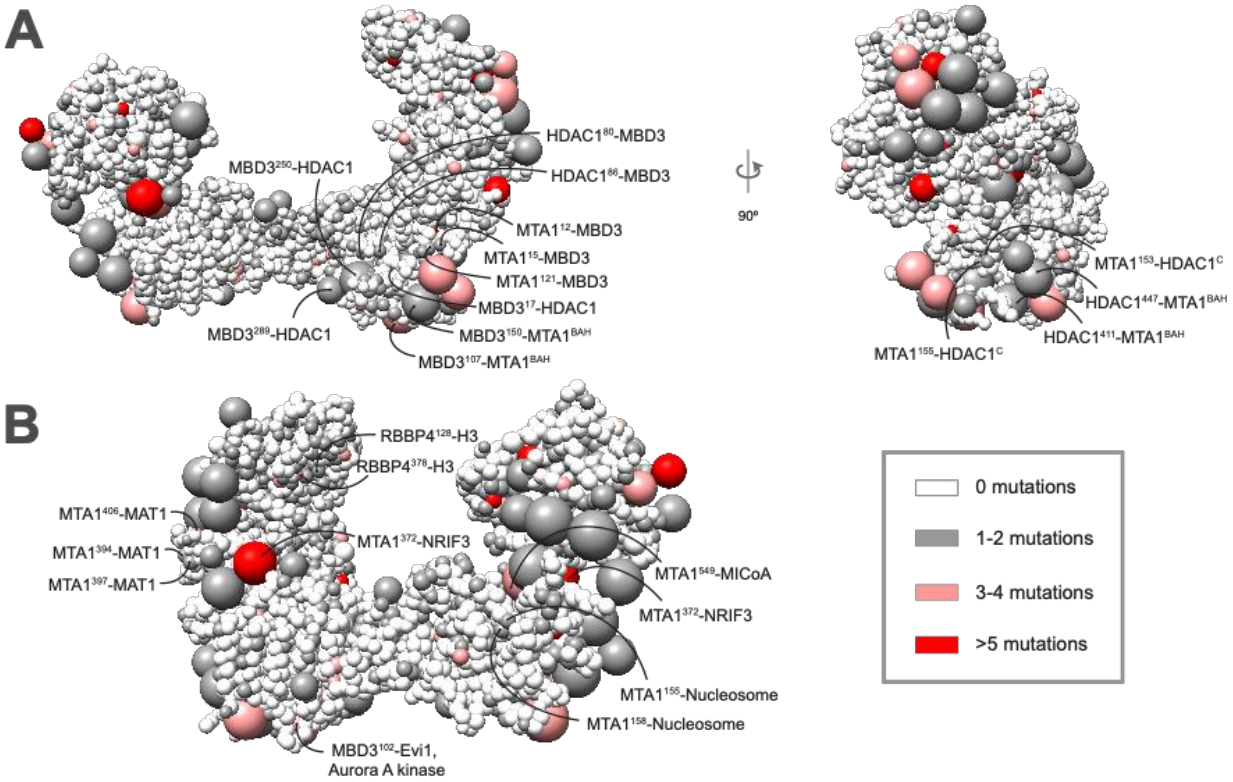

Fig. 5 COSMIC mutations mapped onto the NuDe integrative model. Somatic pathogenic point mutations from the COSMIC database (Forbes et al., 2006) mapped onto the representative bead model of the NuDe complex (Fig. 4A). A. Mutations of residues that map to previously undescribed protein-protein interfaces within our model. Residues from two proteins are at an interface if the average distance between their corresponding bead surfaces is less than 10 Å in the cluster of NuDe integrative models. B. Mutations on residues that map to exposed binding sites between modeled proteins and known binding partners. A bead is colored according to the maximum number of mutations on any residue in the bead, according to the legend. Representative mutations are labeled in both A. and B. See also Table S1 and Fig. S13.

Docking the nucleosome

We next attempted to dock the CHD4-nucleosome structure (Farnung et al., 2020) into the cleft in the NuDe structure between the MTA1 C-terminal arms (Fig. 6). Although there are limitations to this docking (for example, it is a coarse placement, lacks histone tail densities, and binding sites for the nucleosome outside the cleft might also exist), this positioning of the nucleosome

371 indicates its size complementarity to the integrative model, further corroborating the latter. This
372 placement allows for the histone H3 and H4 tails to be located towards the HDAC1 active site.
373 It also accommodates the known interactions between the RBBPs and the histone H3 (Fig. 6).
374 The partial CHD4 structure is exposed. MTA1^{mid}, which contains the zinc finger, can also
375 potentially interact with the nucleosome in this position. Finally, MBD3 does not interact with
376 the nucleosome, since MBD3^{MBD} is buried in NuDe (Fig. 4A-4C), consistent with MBD3 in NuRD
377 failing to bind DNA in immuno-precipitation experiments (Zhang et al., 1999).
378

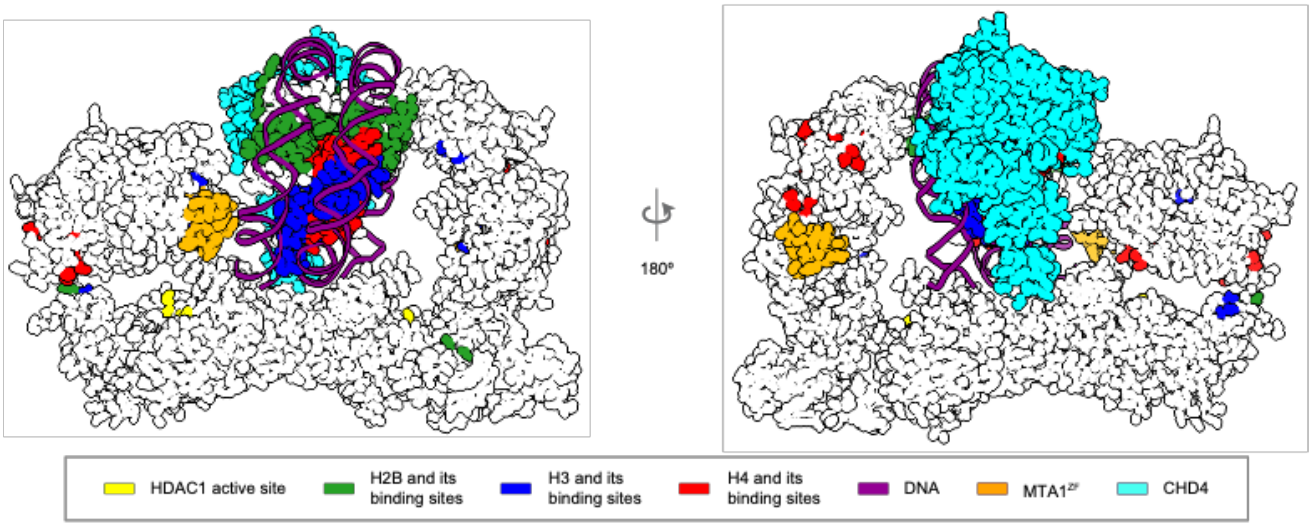

379
380
381 **Fig. 6 Integrative model of NuDe complex with the nucleosome** The CHD4- nucleosome structure (Farnung
382 et al., 2020) is placed in the cleft of the NuDe integrative model. The regions with known atomic structure are
383 shown in the NuDe integrative model from Fig. 4A. Nucleosome proteins/DNA and the corresponding NuDe
384 subunit residues they are known to bind to, are depicted in the same color, as given by the legend.

385 # Discussion

386 Here, we obtained structural models of the MTA1-HDAC1-RBBP4 (MHR), MTA1^{N}-HDAC1-
387 MBD3 (MHM), and MTA1-HDAC1-RBBP4-MBD3-GATAD2 (NuDe) complexes using Bayesian
388 integrative modeling. The approach allowed us to combine all available structural information,
389 including data from SEC-MALLS, DIA-MS, chemical crosslinking mass spectrometry (XLMS),
390 negative stain EM, X-ray crystallography, NMR spectroscopy, secondary structure, and
391 homology predictions (Methods, Fig. 1) (Alqarni et al., 2014; Connelly et al., 2006; Cramer et
392 al., 2014; Gnanapragasam et al., 2011; Low et al., 2020; Millard et al., 2016, 2013; Söding et
393 al., 2005; Tjandra et al., 1997). The models were corroborated by independent cryo-EM maps,
394 enzyme assays, mutagenesis, co-immunoprecipitation studies, and the mapping of cancer
395 mutations (Fig. 5, Fig. S13, Table S1) (Desai et al., 2015; Forbes et al., 2006; Millard et al.,
396 2020; Pflum et al., 2001; Zhang et al., 1999). Importantly, our approach allowed us to localize
397 regions of unknown structure, for *e.g.*, HDAC1^{C} and MBD3^{IDR}, in context of regions of known
398 structure, for *e.g.*, the MTA1-HDAC1 dimer, resulting in the most complete structural
399 characterization of these NuRD sub-complexes so far.
400

401 ## NuDe complex is more ordered than MHR

402 A comparison of MTA1 and RBBP4 in the MHR and NuDe models suggests that these subunits
403 are more conformationally heterogenous in MHR, as shown by the broader localization
404 probability densities for the C-terminal half of MTA1 and RBBPs in MHR (volume enclosed by
405 the corresponding maps = 1120 nm3) compared to NuDe (volume enclosed = 883.6 nm3) (Fig.

S12). Also, the cross-correlation of the MHR localization probability density to the corresponding EM map is lower than that of NuDe, indicating higher heterogeneity for the former. This indicates that the MHR is initially dynamic and the presence of MBD3-GATAD2 possibly makes it less dynamic.

MBD3^{IDR} – MTA1^{dimer} interaction

In our MHM models, one MBD3^{IDR} is near the MTA1^{dimer}, consistent with the previously predicted localization of MBD3^{IDR} based on chemical crosslinks (Low et al., 2020) and MBD2^{IDR} based on a cryo-electron density map (Fig. 3C-3E) (Millard et al., 2020). Two separate mutagenesis and co-immunoprecipitation studies have shown that the MBD^{IDR} and the MTA1 dimerization interface are each essential for MBD2 interaction with the MTA1-HDAC1 dimer (Desai et al., 2015; Millard et al., 2020). Despite the corresponding region of MBD2 being disordered in solution (Desai et al., 2015), MBD3$^{125-175}$ is predicted to be ordered based on PONDR® analysis (Fig. S14) (http://www.pondr.com) (Romero et al., 2001, 1997). Because this region is well conserved across species (Cramer et al., 2017), it is likely that it becomes ordered upon binding, similar to the region of MTA1 that winds irregularly across the surface of HDAC1 (MTA1$^{165-226}$). Further, the crosslinks between MBD3^{IDR} and MTA1 involve a loop (MTA1$^{229-236}$) of the MTA1^{dimer} that is not visible in the MTA1-HDAC1 crystal structure. It is possible that this region of MTA1 may also become ordered upon binding MBD3.

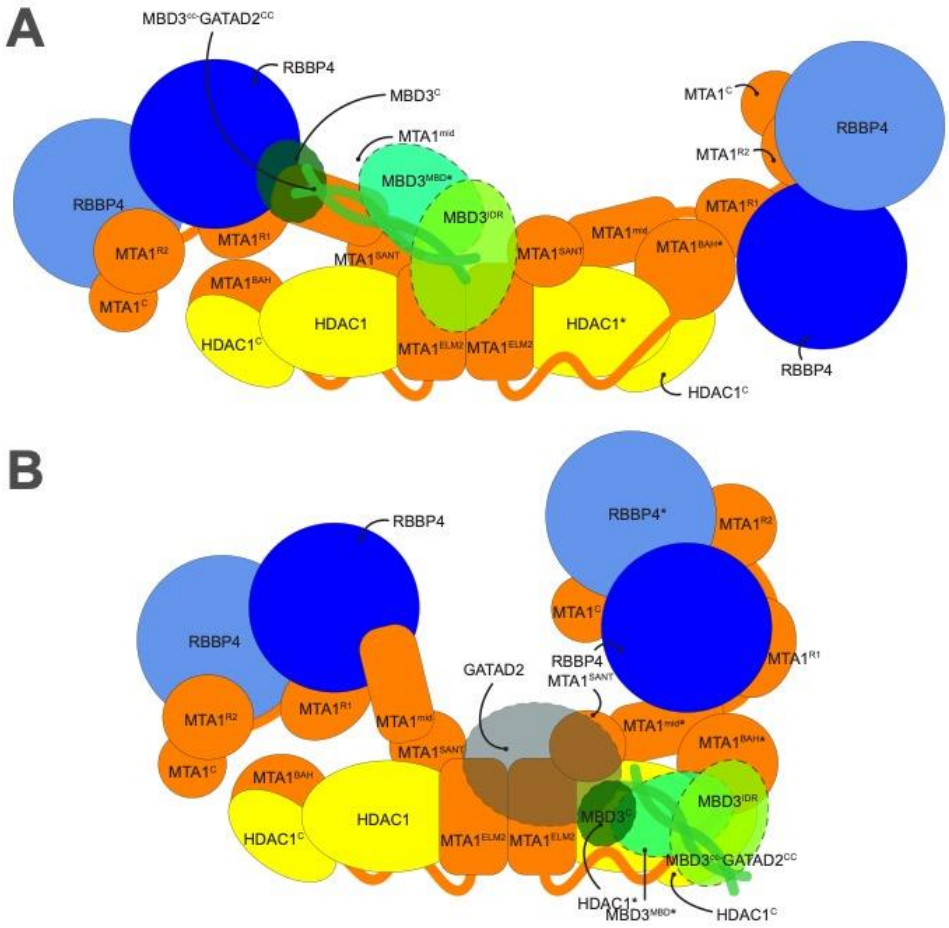

Fig. 7 Bind-and-shift model of MBD3 binding to MHR The figure shows two stages of MBD3 assembly in NuRD. A. In the first stage, the MTA1 dimerization interface is accessible for MBD3^{IDR} to bind. B. In the second stage, upon binding, MBD3 recruits GATAD2 and the chromatin remodeling module and shifts to one end of the MTA1-HDAC1 dimer. GATAD2 localizes near MTA1dimer, precluding a second MBD3 from binding to it.

Bind-and-shift model of MBD3 binding to MHR

The stoichiometry of MBD3 in NuRD is intriguing. The MHM complex has two copies of MBD3, while a single MBD3 is seen in the NuDe and NuRD complexes (Low et al., 2020). Based on our integrative models, we propose a two-stage mechanism to explain the asymmetric binding of MBD3 in NuRD (Fig. 7).

In the first stage (Fig. 7A), the C-terminal arms of MTA1 in MHR are heterogenous and adopt a range of configurations including an extended, open state (Millard et al., 2020) and crossed-over state (Fig. 2, MHR models). In the open state, the MTA1 dimerization interface is accessible for $MBD3^{IDR}$ to bind. This interaction of $MBD3^{IDR}$ with the $MTA1^{dimer}$ is also observed in a cryo-EM study on MTA1:HDAC1:MBD2 and is known to be critical for MBD recruitment to the deacetylase module (Fig. 3, MHM models) (Desai et al., 2015; Millard et al., 2020).

In the second stage (Fig. 7B), upon binding to $MTA1^{dimer}$, MBD3 recruits GATAD2 and the chromatin remodeling module and shifts to one end of the MTA1-HDAC1 dimer (Fig. 4, NuDe models). In this state, GATAD2 localizes near $MTA1^{dimer}$, precluding a second MBD3 from binding to it. Although we did not model full GATAD2 in NuDe due to unavailability of structures and crosslinks involving the protein, the proximity of CHD4, and hence GATAD2, to the $MTA1^{dimer}$ in our coarse nucleosome docking supports this idea (Fig. 6). This possibly explains how GATAD2 introduces asymmetry of MBD3 binding in NuRD. Moreover, upon binding the chromatin remodeling module, the C-terminal arms of MTA1 with the RBBPs are less heterogenous and adopt a closed configuration (Fig. 4, Fig. S12).

The novel NuRD protein interfaces predicted by our model need to be confirmed by future experiments. High-resolution structures of regions such as $MBD3^{IDR}$ will delineate their roles in NuRD. Ultimately, a complete atomic characterization of the NuRD complex will aid in understanding NuRD-mediated regulation of gene expression.

Materials and Methods

Integrative modeling

The integrative structure determination of the NuRD sub-complexes proceeded through four stages (Fig. 1) (Alber et al., 2007; Rout and Sali, 2019; Russel et al., 2012). The modeling protocol (i.e., stages 2, 3, and 4) was scripted using the Python Modeling Interface (PMI) package, a library for modeling macromolecular complexes based on open-source Integrative Modeling Platform (IMP) package, version 2.13.0 (https://integrativemodeling.org) (Russel et al., 2012). The current procedure is an updated version of previously described protocols (Ganesan et al., 2020; Gutierrez et al., 2020; Kim et al., 2018; Saltzberg et al., 2019, 2021; Viswanath et al., 2017a; Webb et al., 2018).

Stage 1: Gathering data

The stoichiometry and isoforms of subunits was based on DIA-MS and SEC-MALLS experiments (Fig. S1) (Low et al., 2020). Known atomic structures were used for the MTA1-HDAC1 dimer, $MTA1^{R1}$ and $MTA1^{R2}$ domains in complex with RBBP4, and MBD domain of MBD3 (Fig. S1) (Alqarni et al., 2014; Cramer et al., 2014; Millard et al., 2016, 2013). The $MTA1^{BAH}$ domain, $MTA1^{H}$, $MTA1^{ZF}$, and $MBD3^{CC}$-$GATAD2A^{CC}$ structures were homology-

modeled based on the structures of related templates (Fig. S1A) (Connelly et al., 2006; Gnanapragasam et al., 2011; Tjandra et al., 1997).

The shapes of the complexes were based on 3D negative-stain EM maps; MHR: to be deposited (24.56 Å), MHM: EMD-21382 (20 Å), and NuDe: EMD-22904 (20 Å) (Low et al., 2020). The negative-stained EM map for the MHR complex was produced by further analysis of data reported in a previous study (Fig. S2) (Low et al., 2020). 25,155 particle images were subjected to multiple rounds of 2D classification in CryoSparc (Punjani et al., 2017), following which an *ab initio* 3D reconstruction was obtained and refined by homogenous 3D refinement. The final map was produced from 13,299 particles and had an estimated resolution of ~25 Å according to the FSC0.143 criterion.

Chemical crosslinks informed the relative localization of the NuRD subunits. A total of 936 crosslinks, including 877 BS3DSS (bis(sulfosuccinimidyl)suberate - disuccinimidyl suberate), 40 DMTMM (dimethoxy triazinyl methyl-morpholinium chloride), and 19 ADH (adipic acid dihydrazide) crosslinks were used (Low et al., 2020). The models were validated by independent EM maps (Millard et al., 2020), biochemical assays (Desai et al., 2015; Pflum et al., 2001; Zhang et al., 1999), and human cancer-associated mutations on NuRD proteins (Forbes et al., 2006).

Stage 2: Representing the system and translating data into spatial restraints

The stoichiometry and representation of subunits is shown (Fig. S1). The domains with known atomic structures were represented in a multi-scale manner with 1 and 10 residues per bead to maximize computational efficiency. These domains were modeled as rigid bodies where the relative distances between beads is constrained during sampling. In contrast, domains without known structure were coarse-grained at 30 residues per bead and modeled as flexible strings of beads.

We next encoded the spatial restraints into a scoring function based on the information gathered in Stage 1, as follows:

(1) *Cross-link restraints:* The Bayesian cross-links restraint (Rieping et al., 2005) was used to restrain the distances spanned by the cross-linked residues (Shi et al., 2014).

(2) *EM restraints:* The Bayesian EM density restraint was used to restrain the shape of the modeled complexes and was based on the cross-correlation between the Gaussian Mixture Model (GMM) representations of the NuRD subunits and the GMM representation of the corresponding negative-stain EM density maps (Bonomi et al., 2019).

(3) *Excluded volume restraints*: The excluded volume restraints were applied to each bead, using the statistical relationship between the volume and the number of residues that it covered (Alber et al., 2007).

(4) *Sequence connectivity restraints*: We applied the sequence connectivity restraints, using a harmonic upper distance bound on the distance between consecutive beads in a subunit, with a threshold distance equal to twice the sum of the radii of the two connected beads. The bead radius was calculated from the excluded volume of the corresponding bead, assuming standard protein density (Shi et al., 2014).

Stage 3: Structural sampling to produce an ensemble of structures that satisfies the restraints

We aimed to maximize the precision at which the sampling of good-scoring solutions was exhaustive (Stage 4). The sampling runs relied on Gibbs sampling, based on the Replica Exchange Monte Carlo algorithm (Saltzberg et al., 2019, 2021). The positions of the rigid bodies (domains with known structure) and flexible beads (domains with unknown structure) were sampled.

The initial positions of the flexible beads and rigid bodies in all complexes were randomized, with one exception. For MHR, we were able to unambiguously dock the structure of the MTA1-HDAC1 core in the EM map, with the help of the previous EM map (EMD-3399) (Millard et al., 2016). Hence the position of the corresponding rigid body was fixed throughout.

The Monte Carlo moves included random translations of individual beads in the flexible segments and rigid bodies (around 3.7 Å and 1.3 Å respectively). A model was saved every 10 Gibbs sampling steps, each consisting of a cycle of Monte Carlo steps that moved every bead and rigid body once.

The sampling produced a total of 40 million MHR, 48 million MHM, and 80 million NuDe integrative models.

Stage 4: Analysing and validating the ensemble of structures and data

The sampled models were analysed to assess sampling exhaustiveness and estimate the precision of the structure, its consistency with input data and consistency with data not used in modeling. The structure was further validated by experiments based on the predictions from the models. We used the analysis and validation protocol published earlier (Rout and Sali, 2019; Saltzberg et al., 2019, 2021; Viswanath et al., 2017b). Assessment began with a test of the thoroughness of structural sampling, including structural clustering of the models, estimating model precision, and visualizing the variability in the ensemble of structures using localization probability density maps (Viswanath et al., 2017b). The precision of a domain refers to its positional variation in an ensemble of superposed models. It can also be visualized by the localization probability density map for the domain. A localization probability density map specifies the probability of a voxel (3D volume unit) being occupied by a bead in a set of superposed models. The models and densities were visualized with UCSF Chimera and ChimeraX (Pettersen et al., 2021, 2004).

(1) *Determining good-scoring models*

Starting from the millions of sampled models, first, we selected models obtained after score equilibration and clustered them based on the restraint scores (Saltzberg et al., 2021). For further analysis, we considered 15200 MHR, 21960 MHM, and 21632 NuDe good-scoring models that satisfy the data restraints sufficiently well.

(2) *Clustering and structure precision*

We next assessed the sampling exhaustiveness and performed structural clustering (Saltzberg et al., 2019, 2021; Viswanath et al., 2017b). Integrative structure determination resulted in effectively a single cluster for all complexes, at a precision of 26.8 Å (MHR), 23.8 Å (MHM), and 34.6 Å (NuDe). The cluster precision is the bead RMSD from the cluster centroid model averaged over all models in the cluster (Viswanath et al., 2017b).

570
571 (3) *Fit to input information*
572 The dominant clusters from each modeled NuRD sub-complex satisfied over 95% of all the
573 BS3DSS, ADH, and DMTMM crosslinks used; a crosslink is satisfied by a cluster of models if
574 the corresponding Cα-Cα distance in any model in the cluster is less than 35Å, 35Å, 25Å for
575 BS3DSS, ADH, and DMTMM crosslinks respectively. The agreement between the models and
576 the corresponding EM maps was computed by calculating the cross-correlation of the combined
577 localization probability densities of all subunits for the major cluster with the experimental EM
578 map using the *fitmap* tool in UCSF Chimera (Fig. 2-4) (Pettersen et al., 2004). The remainder
579 of the restraints are harmonic, with a specified standard deviation. The cluster generally
580 satisfied the excluded volume and sequence connectivity restraints. A restraint is satisfied by a
581 cluster of models if the restrained distance in any model in the cluster (considering restraint
582 ambiguity) is violated by less than 3 standard deviations, specified for the restraint. Most of the
583 violations are small, and can be rationalized by local structural fluctuations, coarse-grained
584 representation of the model, and/or finite structural sampling.
585
586 (4) *Fit to data not used in modeling*
587 The MHR integrative models were supported by histone deacetylation assays, mutagenesis,
588 and co-immunoprecipitation showing that MTA1 and the $HDAC1^{C}$ regulate HDAC1 deacetylase
589 activity and NuRD assembly (Pflum et al., 2001; Zhang et al., 1999). The localization of domains
590 such as $MTA1^{BAH}$ and RBBP4 were validated by their consistency with independently
591 determined cryo-EM maps (Millard et al., 2020).
592
593 The MHM integrative models were supported by independent cryo-EM maps of the complex
594 showing similar localizations for $MBD2^{MBD}$ and $MTA1^{BAH}$ (Millard et al., 2020). The $MBD3^{IDR}$-
595 $MTA1^{dimer}$ interaction was also supported by two separate mutagenesis and co-
596 immunoprecipitation studies (Desai et al., 2015; Millard et al., 2020).
597
598 The NuDe integrative models were corroborated by immunoprecipitation experiments showing
599 that the MBD domain of MBD3 is buried in NuRD (Zhang et al., 1999). They were also
600 supported by independent cryo-EM maps showing that MBD3 is proximal to $MTA1^{BAH}$, and
601 biochemical assays showing the importance of $HDAC1^{C}$ interactions in NuRD (Millard et al.,
602 2020; Pflum et al., 2001). The mapping of cancer mutations to protein-protein interfaces in the
603 NuDe model also supported them (Fig. 5, Fig. S13, Table S1) (Forbes et al., 2006).
604
605 *4.1 Mapping COSMIC mutations*
606 We obtained a total of 356 somatic, confirmed pathogenic, point mutations for the modeled
607 NuRD subunits (MTA1, HDAC1, RBBP4, MBD3) from the COSMIC (Catalogue of Somatic
608 Mutations in Cancer) database (Forbes et al., 2006). For each subunit, point mutations were
609 selected from search results based on the presence of census genes and correct
610 documentation of current structures. To ensure the mutations studied significantly affect the
611 function, folding, and protein-protein interaction of the protein, the “confirmed pathogenic” and
612 “somatic” filters were applied in all cases.
613
614

Acknowledgements

We thank Vinothkumar Kutti Ragunath for useful comments on the manuscript.

Molecular graphics images were produced using the UCSF Chimera and UCSF ChimeraX packages from the Resource for Biocomputing, Visualization, and Informatics at the University of California, San Francisco (supported by NIH P41 RR001081).

Funding

This work has been supported by the following grants: Department of Atomic Energy (DAE) TIFR grant RTI 4006 and Department of Science and Technology (DST) SERB grant SPG/2020/000475 from the Government of India to S.V, National Health and Medical Research Council of Australia project grants: APP1012161, APP1063301, APP1126357 to M.J.L. and J.P.M. and a fellowship (APP1058916) from the same organization to J.P.M.

Conflict of Interest

None declared.

References

Alber, F., Dokudovskaya, S., Veenhoff, L.M., Zhang, W., Kipper, J., Devos, D., Suprapto, A., Karni-Schmidt, O., Williams, R., Chait, B.T., Rout, M.P., Sali, A., 2007. Determining the architectures of macromolecular assemblies. Nature 450, 683–694. https://doi.org/10.1038/nature06404

Alqarni, S.S.M., Murthy, A., Zhang, W., Przewloka, M.R., Silva, A.P.G., Watson, A.A., Lejon, S., Pei, X.Y., Smits, A.H., Kloet, S.L., Wang, H., Shepherd, N.E., Stokes, P.H., Blobel, G.A., Vermeulen, M., Glover, D.M., Mackay, J.P., Laue, E.D., 2014. Insight into the Architecture of the NuRD Complex. J. Biol. Chem. 289, 21844–21855. https://doi.org/10.1074/jbc.M114.558940

Basta, J., Rauchman, M., 2017. Chapter 3 - The Nucleosome Remodeling and Deacetylase Complex in Development and Disease, in: Laurence, J., Beusekom, M.V. (Eds.), Translating Epigenetics to the Clinic. Academic Press, Boston, pp. 37–72. https://doi.org/10.1016/B978-0-12-800802-7.00003-4

Basta, J., Rauchman, M., 2015. The nucleosome remodeling and deacetylase complex in development and disease. Transl. Res. J. Lab. Clin. Med. 165, 36–47. https://doi.org/10.1016/j.trsl.2014.05.003

Bode, D., Yu, L., Tate, P., Pardo, M., Choudhary, J., 2016. Characterization of Two Distinct Nucleosome Remodeling and Deacetylase (NuRD) Complex Assemblies in Embryonic Stem Cells*. Mol. Cell. Proteomics 15, 878–891. https://doi.org/10.1074/mcp.M115.053207

Bonomi, M., Hanot, S., Greenberg, C.H., Sali, A., Nilges, M., Vendruscolo, M., Pellarin, R., 2019. Bayesian Weighing of Electron Cryo-Microscopy Data for Integrative Structural Modeling. Structure 27, 175-188.e6. https://doi.org/10.1016/j.str.2018.09.011

Bornelöv, S., Reynolds, N., Xenophontos, M., Gharbi, S., Johnstone, E., Floyd, R., Ralser, M., Signolet, J., Loos, R., Dietmann, S., Bertone, P., Hendrich, B., 2018. The Nucleosome Remodeling and Deacetylation Complex Modulates Chromatin Structure at Sites of

659 Active Transcription to Fine-Tune Gene Expression. Mol. Cell 71, 56-72.e4.
660 https://doi.org/10.1016/j.molcel.2018.06.003
661 Burgold, T., Barber, M., Kloet, S., Cramard, J., Gharbi, S., Floyd, R., Kinoshita, M., Ralser, M.,
662 Vermeulen, M., Reynolds, N., Dietmann, S., Hendrich, B., 2019. The Nucleosome
663 Remodelling and Deacetylation complex suppresses transcriptional noise during lineage
664 commitment. EMBO J. 38, e100788. https://doi.org/10.15252/embj.2018100788
665 Connelly, J.J., Yuan, P., Hsu, H.-C., Li, Z., Xu, R.-M., Sternglanz, R., 2006. Structure and
666 Function of the Saccharomyces cerevisiae Sir3 BAH Domain. Mol. Cell. Biol. 26, 3256–
667 3265. https://doi.org/10.1128/MCB.26.8.3256-3265.2006
668 Cramer, J.M., Pohlmann, D., Gomez, F., Mark, L., Kornegay, B., Hall, C., Siraliev-Perez, E.,
669 Walavalkar, N.M., Sperlazza, M.J., Bilinovich, S., Prokop, J.W., Hill, A.L., Williams, D.C.,
670 2017. Methylation specific targeting of a chromatin remodeling complex from sponges
671 to humans. Sci. Rep. 7, 40674. https://doi.org/10.1038/srep40674
672 Cramer, J.M., Scarsdale, J.N., Walavalkar, N.M., Buchwald, W.A., Ginder, G.D., Williams, D.C.,
673 2014. Probing the Dynamic Distribution of Bound States for Methylcytosine-binding
674 Domains on DNA* *This work was supported, in whole or in part, by National Institutes
675 of Health Grants R01 GM098624 (to D. C. W.) and R01 DK029902 (to G. D. G.). NMR
676 data were acquired using NMR instrumentation in the Virginia Commonwealth University
677 Massey Cancer Center Structural Biology Core, and surface plasmon resonance data
678 were acquired in the Virginia Commonwealth University Massey Cancer Center Flow
679 Cytometry Core, both of which are supported, in part, by NCI Cancer Center Core
680 Support Grant P30 CA016059. J. Biol. Chem. 289, 1294–1302.
681 https://doi.org/10.1074/jbc.M113.512236
682 Denslow, S.A., Wade, P.A., 2007. The human Mi-2/NuRD complex and gene regulation.
683 Oncogene 26, 5433–5438. https://doi.org/10.1038/sj.onc.1210611
684 Desai, M.A., Webb, H.D., Sinanan, L.M., Scarsdale, J.N., Walavalkar, N.M., Ginder, G.D.,
685 Williams, D.C., 2015. An intrinsically disordered region of methyl-CpG binding domain
686 protein 2 (MBD2) recruits the histone deacetylase core of the NuRD complex. Nucleic
687 Acids Res. 43, 3100–3113. https://doi.org/10.1093/nar/gkv168
688 Farnung, L., Ochmann, M., Cramer, P., 2020. Nucleosome-CHD4 chromatin remodeler
689 structure maps human disease mutations. eLife 9, e56178.
690 https://doi.org/10.7554/eLife.56178
691 Forbes, S., Clements, J., Dawson, E., Bamford, S., Webb, T., Dogan, A., Flanagan, A., Teague,
692 J., Wooster, R., Futreal, P.A., Stratton, M.R., 2006. Cosmic 2005. Br. J. Cancer 94, 318–
693 322. https://doi.org/10.1038/sj.bjc.6602928
694 Ganesan, S.J., Feyder, M.J., Chemmama, I.E., Fang, F., Rout, M.P., Chait, B.T., Shi, Y.,
695 Munson, M., Sali, A., 2020. Integrative structure and function of the yeast exocyst
696 complex. Protein Sci. Publ. Protein Soc. 29, 1486–1501.
697 https://doi.org/10.1002/pro.3863
698 Gnanapragasam, M.N., Scarsdale, J.N., Amaya, M.L., Webb, H.D., Desai, M.A., Walavalkar,
699 N.M., Wang, S.Z., Zu Zhu, S., Ginder, G.D., Williams, D.C., 2011. p66α–MBD2 coiled-
700 coil interaction and recruitment of Mi-2 are critical for globin gene silencing by the MBD2–
701 NuRD complex. Proc. Natl. Acad. Sci. 108, 7487–7492.
702 Guo, T., Luna, A., Rajapakse, V.N., Koh, C.C., Wu, Z., Liu, W., Sun, Y., Gao, H., Menden, M.P.,
703 Xu, C., Calzone, L., Martignetti, L., Auwerx, C., Buljan, M., Banaei-Esfahani, A., Ori, A.,
704 Iskar, M., Gillet, L., Bi, R., Zhang, J., Zhang, H., Yu, C., Zhong, Q., Varma, S., Schmitt,
705 U., Qiu, P., Zhang, Q., Zhu, Y., Wild, P.J., Garnett, M.J., Bork, P., Beck, M., Liu, K.,
706 Saez-Rodriguez, J., Elloumi, F., Reinhold, W.C., Sander, C., Pommier, Y., Aebersold,

R., 2019. Quantitative Proteome Landscape of the NCI-60 Cancer Cell Lines. iScience 21, 664–680. https://doi.org/10.1016/j.isci.2019.10.059

Gutierrez, C., Chemmama, I.E., Mao, H., Yu, C., Echeverria, I., Block, S.A., Rychnovsky, S.D., Zheng, N., Sali, A., Huang, L., 2020. Structural dynamics of the human COP9 signalosome revealed by cross-linking mass spectrometry and integrative modeling. Proc. Natl. Acad. Sci. 117, 4088–4098. https://doi.org/10.1073/pnas.1915542117

Hoffmann, A., Spengler, D., 2019. Chromatin Remodeling Complex NuRD in Neurodevelopment and Neurodevelopmental Disorders. Front. Genet. 0. https://doi.org/10.3389/fgene.2019.00682

Hong, W., Nakazawa, M., Chen, Y.-Y., Kori, R., Vakoc, C.R., Rakowski, C., Blobel, G.A., 2005. FOG-1 recruits the NuRD repressor complex to mediate transcriptional repression by GATA-1. EMBO J. 24, 2367–2378. https://doi.org/10.1038/sj.emboj.7600703

Jumper, J., Evans, R., Pritzel, A., Green, T., Figurnov, M., Ronneberger, O., Tunyasuvunakool, K., Bates, R., Žídek, A., Potapenko, A., Bridgland, A., Meyer, C., Kohl, S.A.A., Ballard, A.J., Cowie, A., Romera-Paredes, B., Nikolov, S., Jain, R., Adler, J., Back, T., Petersen, S., Reiman, D., Clancy, E., Zielinski, M., Steinegger, M., Pacholska, M., Berghammer, T., Bodenstein, S., Silver, D., Vinyals, O., Senior, A.W., Kavukcuoglu, K., Kohli, P., Hassabis, D., 2021. Highly accurate protein structure prediction with AlphaFold. Nature 596, 583–589. https://doi.org/10.1038/s41586-021-03819-2

Kim, S.J., Fernandez-Martinez, J., Nudelman, I., Shi, Y., Zhang, W., Raveh, B., Herricks, T., Slaughter, B.D., Hogan, J.A., Upla, P., Chemmama, I.E., Pellarin, R., Echeverria, I., Shivaraju, M., Chaudhury, A.S., Wang, J., Williams, R., Unruh, J.R., Greenberg, C.H., Jacobs, E.Y., Yu, Z., de la Cruz, M.J., Mironska, R., Stokes, D.L., Aitchison, J.D., Jarrold, M.F., Gerton, J.L., Ludtke, S.J., Akey, C.W., Chait, B.T., Sali, A., Rout, M.P., 2018. Integrative structure and functional anatomy of a nuclear pore complex. Nature 555, 475–482. https://doi.org/10.1038/nature26003

Kloet, S.L., Baymaz, H.I., Makowski, M., Groenewold, V., Jansen, P.W.T.C., Berendsen, M., Niazi, H., Kops, G.J., Vermeulen, M., 2015. Towards elucidating the stability, dynamics and architecture of the nucleosome remodeling and deacetylase complex by using quantitative interaction proteomics. FEBS J. 282, 1774–1785. https://doi.org/10.1111/febs.12972

Lejon, S., Thong, S.Y., Murthy, A., AlQarni, S., Murzina, N.V., Blobel, G.A., Laue, E.D., Mackay, J.P., 2011. Insights into Association of the NuRD Complex with FOG-1 from the Crystal Structure of an RbAp48·FOG-1 Complex *. J. Biol. Chem. 286, 1196–1203. https://doi.org/10.1074/jbc.M110.195842

Li, D.-Q., Kumar, R., 2010. Mi-2/NuRD complex making inroads into DNA-damage response pathway. Cell Cycle Georget. Tex 9, 2071–2079. https://doi.org/10.4161/cc.9.11.11735

Low, J.K.K., Silva, A.P.G., Sharifi Tabar, M., Torrado, M., Webb, S.R., Parker, B.L., Sana, M., Smits, C., Schmidberger, J.W., Brillault, L., Jackman, M.J., Williams, D.C., Blobel, G.A., Hake, S.B., Shepherd, N.E., Landsberg, M.J., Mackay, J.P., 2020. The Nucleosome Remodeling and Deacetylase Complex Has an Asymmetric, Dynamic, and Modular Architecture. Cell Rep. 33, 108450. https://doi.org/10.1016/j.celrep.2020.108450

Millard, C.J., Fairall, L., Ragan, T.J., Savva, C.G., Schwabe, J.W.R., 2020. The topology of chromatin-binding domains in the NuRD deacetylase complex. Nucleic Acids Res. 48, 12972–12982. https://doi.org/10.1093/nar/gkaa1121

Millard, C.J., Varma, N., Saleh, A., Morris, K., Watson, P., Bottrill, A., Fairall, L., Smith, C., Schwabe, J., 2016. The structure of the core NuRD repression complex provides insights into its interaction with chromatin. ELife 2016. https://doi.org/10.7554/eLife.13941

755 Millard, C.J., Watson, P.J., Celardo, I., Gordiyenko, Y., Cowley, S.M., Robinson, C.V., Fairall,
756 L., Schwabe, J.W.R., 2013. Class I HDACs Share a Common Mechanism of Regulation
757 by Inositol Phosphates. Mol. Cell 51, 57–67.
758 https://doi.org/10.1016/j.molcel.2013.05.020
759 Pettersen, E.F., Goddard, T.D., Huang, C.C., Couch, G.S., Greenblatt, D.M., Meng, E.C.,
760 Ferrin, T.E., 2004. UCSF Chimera--a visualization system for exploratory research and
761 analysis. J. Comput. Chem. 25, 1605–1612. https://doi.org/10.1002/jcc.20084
762 Pettersen, E.F., Goddard, T.D., Huang, C.C., Meng, E.C., Couch, G.S., Croll, T.I., Morris, J.H.,
763 Ferrin, T.E., 2021. UCSF ChimeraX: Structure visualization for researchers, educators,
764 and developers. Protein Sci. 30, 70–82. https://doi.org/10.1002/pro.3943
765 Pflum, M.K.H., Tong, J.K., Lane, W.S., Schreiber, S.L., 2001. Histone Deacetylase 1
766 Phosphorylation Promotes Enzymatic Activity and Complex Formation*. J. Biol. Chem.
767 276, 47733–47741. https://doi.org/10.1074/jbc.M105590200
768 Punjani, A., Rubinstein, J.L., Fleet, D.J., Brubaker, M.A., 2017. cryoSPARC: algorithms for
769 rapid unsupervised cryo-EM structure determination. Nat. Methods 14, 290–296.
770 https://doi.org/10.1038/nmeth.4169
771 Rathert, P., Dhayalan, A., Murakami, M., Zhang, X., Tamas, R., Jurkowska, R., Komatsu, Y.,
772 Shinkai, Y., Cheng, X., Jeltsch, A., 2008. Protein lysine methyltransferase G9a acts on
773 non-histone targets. Nat. Chem. Biol. 4, 344–346. https://doi.org/10.1038/nchembio.88
774 Reynolds, N., O'Shaughnessy, A., Hendrich, B., 2013. Transcriptional repressors: multifaceted
775 regulators of gene expression. Development 140, 505–512.
776 https://doi.org/10.1242/dev.083105
777 Rieping, W., Habeck, M., Nilges, M., 2005. Inferential Structure Determination. Science 309,
778 303–306. https://doi.org/10.1126/science.1110428
779 Romero, P., Obradovic, Z., Kissinger, C., Villafranca, J.E., Dunker, A.K., 1997. Identifying
780 disordered regions in proteins from amino acid sequence, in: Proceedings of
781 International Conference on Neural Networks (ICNN'97). Presented at the Proceedings
782 of International Conference on Neural Networks (ICNN'97), pp. 90–95 vol.1.
783 https://doi.org/10.1109/ICNN.1997.611643
784 Romero, P., Obradovic, Z., Li, X., Garner, E.C., Brown, C.J., Dunker, A.K., 2001. Sequence
785 complexity of disordered protein. Proteins 42, 38–48. https://doi.org/10.1002/1097-
786 0134(20010101)42:1<38::aid-prot50>3.0.co;2-3
787 Rout, M.P., Sali, A., 2019. Principles for Integrative Structural Biology Studies. Cell 177, 1384–
788 1403. https://doi.org/10.1016/j.cell.2019.05.016
789 Russel, D., Lasker, K., Webb, B., Velázquez-Muriel, J., Tjioe, E., Schneidman-Duhovny, D.,
790 Peterson, B., Sali, A., 2012. Putting the Pieces Together: Integrative Modeling Platform
791 Software for Structure Determination of Macromolecular Assemblies. PLoS Biol. 10,
792 e1001244. https://doi.org/10.1371/journal.pbio.1001244
793 Saltzberg, D., Greenberg, C.H., Viswanath, S., Chemmama, I., Webb, B., Pellarin, R.,
794 Echeverria, I., Sali, A., 2019. Modeling Biological Complexes Using Integrative Modeling
795 Platform, in: Bonomi, M., Camilloni, C. (Eds.), Biomolecular Simulations: Methods and
796 Protocols, Methods in Molecular Biology. Springer, New York, NY, pp. 353–377.
797 https://doi.org/10.1007/978-1-4939-9608-7_15
798 Saltzberg, D.J., Viswanath, S., Echeverria, I., Chemmama, I.E., Webb, B., Sali, A., 2021. Using
799 Integrative Modeling Platform to compute, validate, and archive a model of a protein
800 complex structure. Protein Sci. 30, 250–261. https://doi.org/10.1002/pro.3995
801 Schneidman-Duhovny, D., Pellarin, R., Sali, A., 2014. Uncertainty in integrative structural
802 modeling. Curr. Opin. Struct. Biol. 28, 96–104. https://doi.org/10.1016/j.sbi.2014.08.001

803 Sharifi Tabar, M., Mackay, J.P., Low, J.K.K., 2019. The stoichiometry and interactome of the
804 Nucleosome Remodeling and Deacetylase (NuRD) complex are conserved across
805 multiple cell lines. FEBS J. 286, 2043–2061. https://doi.org/10.1111/febs.14800
806 Shi, Y., Fernandez-Martinez, J., Tjioe, E., Pellarin, R., Kim, S.J., Williams, R., Schneidman-
807 Duhovny, D., Sali, A., Rout, M.P., Chait, B.T., 2014. Structural characterization by cross-
808 linking reveals the detailed architecture of a coatomer-related heptameric module from
809 the nuclear pore complex. Mol. Cell. Proteomics MCP 13, 2927–2943.
810 https://doi.org/10.1074/mcp.M114.041673
811 Smeenk, G., Wiegant, W.W., Vrolijk, H., Solari, A.P., Pastink, A., van Attikum, H., 2010. The
812 NuRD chromatin–remodeling complex regulates signaling and repair of DNA damage.
813 J. Cell Biol. 190, 741–749. https://doi.org/10.1083/jcb.201001048
814 Smits, A.H., Jansen, P.W.T.C., Poser, I., Hyman, A.A., Vermeulen, M., 2013. Stoichiometry of
815 chromatin-associated protein complexes revealed by label-free quantitative mass
816 spectrometry-based proteomics. Nucleic Acids Res. 41, e28.
817 https://doi.org/10.1093/nar/gks941
818 Söding, J., Biegert, A., Lupas, A.N., 2005. The HHpred interactive server for protein homology
819 detection and structure prediction. Nucleic Acids Res. 33, W244-248.
820 https://doi.org/10.1093/nar/gki408
821 Spruijt, C.G., Luijsterburg, M.S., Menafra, R., Lindeboom, R.G.H., Jansen, P.W.T.C.,
822 Edupuganti, R.R., Baltissen, M.P., Wiegant, W.W., Voelker-Albert, M.C., Matarese, F.,
823 Mensinga, A., Poser, I., Vos, H.R., Stunnenberg, H.G., van Attikum, H., Vermeulen, M.,
824 2016. ZMYND8 Co-localizes with NuRD on Target Genes and Regulates Poly(ADP-
825 Ribose)-Dependent Recruitment of GATAD2A/NuRD to Sites of DNA Damage. Cell Rep.
826 17, 783–798. https://doi.org/10.1016/j.celrep.2016.09.037
827 Tjandra, N., Omichinski, J.G., Gronenborn, A.M., Clore, G.M., Bax, A., 1997. Use of dipolar 1H-
828 15N and 1H-13C couplings in the structure determination of magnetically oriented
829 macromolecules in solution. Nat. Struct. Biol. 4, 732–738.
830 https://doi.org/10.1038/nsb0997-732
831 Toh, Y., Nicolson, G.L., 2009. The role of the MTA family and their encoded proteins in human
832 cancers: molecular functions and clinical implications. Clin. Exp. Metastasis 26, 215–
833 227. https://doi.org/10.1007/s10585-008-9233-8
834 Viswanath, S., Bonomi, M., Kim, S.J., Klenchin, V.A., Taylor, K.C., Yabut, K.C., Umbreit, N.T.,
835 Van Epps, H.A., Meehl, J., Jones, M.H., Russel, D., Velazquez-Muriel, J.A., Winey, M.,
836 Rayment, I., Davis, T.N., Sali, A., Muller, E.G., 2017a. The molecular architecture of the
837 yeast spindle pole body core determined by Bayesian integrative modeling. Mol. Biol.
838 Cell 28, 3298–3314. https://doi.org/10.1091/mbc.E17-06-0397
839 Viswanath, S., Chemmama, I.E., Cimermancic, P., Sali, A., 2017b. Assessing Exhaustiveness
840 of Stochastic Sampling for Integrative Modeling of Macromolecular Structures. Biophys.
841 J. 113, 2344–2353. https://doi.org/10.1016/j.bpj.2017.10.005
842 Ward, A.B., Sali, A., Wilson, I.A., 2013. Integrative Structural Biology. Science 339, 913–915.
843 https://doi.org/10.1126/science.1228565
844 Webb, B., Viswanath, S., Bonomi, M., Pellarin, R., Greenberg, C.H., Saltzberg, D., Sali, A.,
845 2018. Integrative structure modeling with the Integrative Modeling Platform. Protein Sci.
846 27, 245–258. https://doi.org/10.1002/pro.3311
847 Yoshida, T., Hazan, I., Zhang, J., Ng, S.Y., Naito, T., Snippert, H.J., Heller, E.J., Qi, X., Lawton,
848 L.N., Williams, C.J., Georgopoulos, K., 2008. The role of the chromatin remodeler Mi-2β
849 in hematopoietic stem cell self-renewal and multilineage differentiation. Genes Dev. 22,
850 1174–1189. https://doi.org/10.1101/gad.1642808

851 Zhang, W., Aubert, A., Gomez de Segura, J.M., Karuppasamy, M., Basu, S., Murthy, A.S.,
852 Diamante, A., Drury, T.A., Balmer, J., Cramard, J., Watson, A.A., Lando, D., Lee, S.F.,
853 Palayret, M., Kloet, S.L., Smits, A.H., Deery, M.J., Vermeulen, M., Hendrich, B.,
854 Klenerman, D., Schaffitzel, C., Berger, I., Laue, E.D., 2016. The Nucleosome
855 Remodeling and Deacetylase Complex NuRD Is Built from Preformed Catalytically
856 Active Sub-modules. J. Mol. Biol. 428, 2931–2942.
857 https://doi.org/10.1016/j.jmb.2016.04.025
858 Zhang, Y., Ng, H.-H., Erdjument-Bromage, H., Tempst, P., Bird, A., Reinberg, D., 1999.
859 Analysis of the NuRD subunits reveals a histone deacetylase core complex and a
860 connection with DNA methylation. Genes Dev. 13, 1924–1935.
861

Supplementary Figures and Tables

Molecular architecture of nucleosome remodeling and deacetylase sub-complexes by integrative structure determination

Shreyas Arvindekar[1], Matthew J. Jackman[2], Jason K.K. Low[3], Michael J. Landsberg[2, *], Joel P. Mackay[3, *], and Shruthi Viswanath[1, *]

[1]National Center for Biological Sciences, Tata Institute of Fundamental Research, Bangalore, India

[2]School of Chemistry and Molecular Biosciences, University of Queensland, QLD, Australia

[3]School of Life and Environmental Sciences, University of Sydney, NSW, Australia

*Corresponding authors E-mail: m.landsberg@uq.edu.au (M.J.L.); joel.mackay@sydney.edu.au (J.P.M.); shruthiv@ncbs.res.in (S.V.)

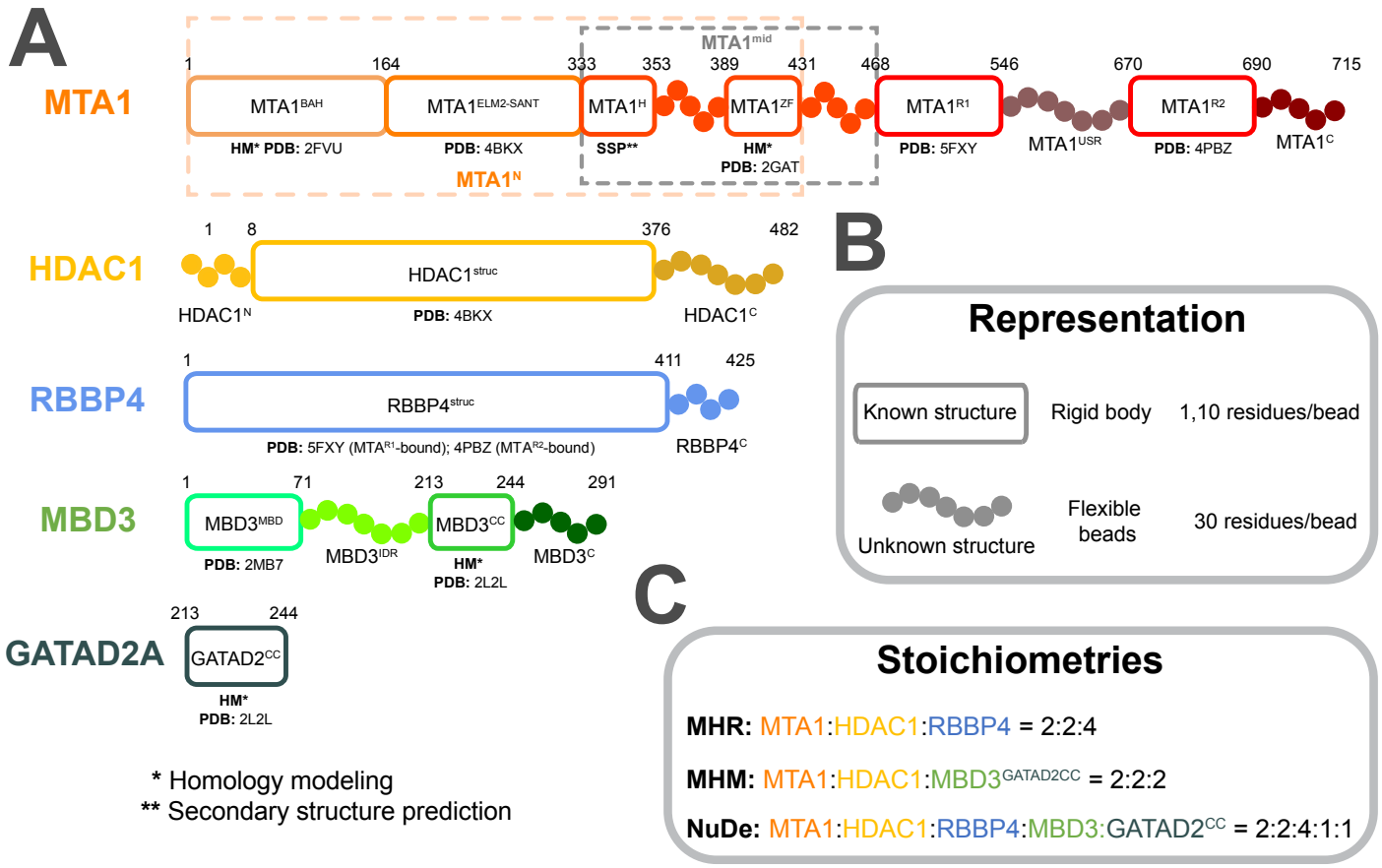

Fig. S1 Subunits in NuRD sub-complexes A. Sequences and isoforms of modeled subunits are shown and domains are labeled. Domains are shown in progressively dark shades along the sequence for MTA1, HDAC1, and MBD3. Regions with known structure are represented by rectangles while regions without known structure are represented by beads. PDB IDs are shown for existing subunit structures and templates of homology models. B. Coarse-grained bead representation of subunits and C. stoichiometries of modeled complexes.

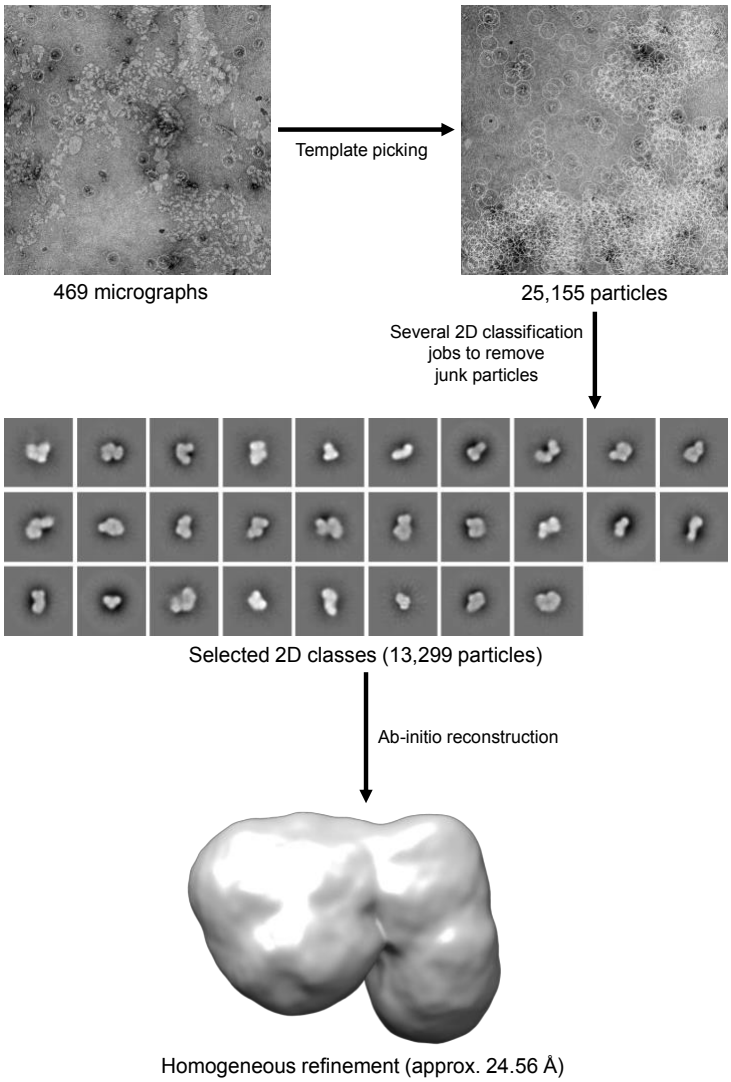

Fig. S2 Single particle analysis of the MHR complex. A flowthrough from the micrographs imported into Cryosparc (Punjani et al., 2017) to the final 3D reconstruction of the MHR complex using the ab-initio reconstruction job. 2D classes were generated using 50 classes per run, with particles from non-junk classes used as input to subsequent 2D classification jobs. Non-uniform refinement was not performed on the final structure due to its low resolution.

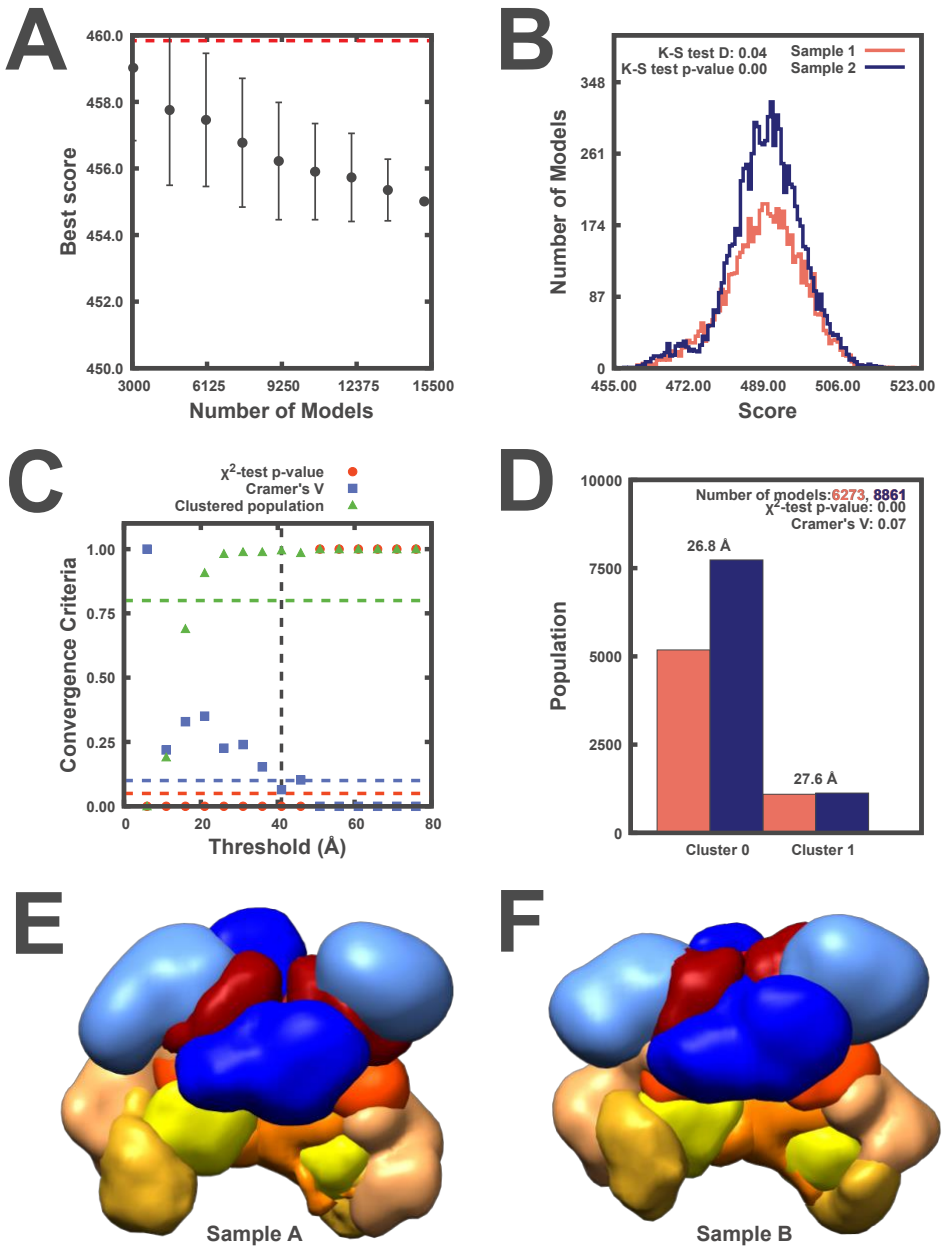

Fig. S3 Sampling exhaustiveness protocol on MHR models Results of test 1, convergence of the model score, for the 15200 good-scoring models; the scores do not continue to improve as more models are computed essentially independently. The error bar represents the standard deviations of the best scores, estimated by repeating sampling of models 10 times. The red dotted line indicates a lower bound reference on the total score. B. Results of test 2, testing similarity of model score distributions between samples 1 (red) and 2 (blue); the difference in the distribution of scores is significant (Kolmogorov-Smirnov two-sample test p-value less than 0.05) but the magnitude of the difference is small (the Kolmogorov-Smirnov two-sample test statistic D is 0.04); thus, the two score distributions are effectively equal. C. Results of test 3, three criteria for determining the sampling precision (Y-axis), evaluated as a function of the RMSD clustering threshold (X-axis). First, the p-value is computed using the χ^2 -test for homogeneity of proportions (red dots). Second, an effect size for the χ^2-test is quantified by the Cramer's V value (blue squares). Third, the population of models in sufficiently large clusters (containing at least 10 models from each sample) is shown as green triangles. The vertical dotted grey line indicates the RMSD clustering threshold at which three conditions are satisfied (p-value > 0.05 [dotted red line], Cramer's V < 0.10 [dotted blue line], and the population of clustered models > 0.80 [dotted green line]), thus defining the sampling precision of 41 Å. D. Populations of sample 1 and 2 models in the clusters obtained by threshold-based clustering using the RMSD threshold of 41 Å. Cluster precision is shown for each cluster. E. and F. Results of test 4: comparison of localization probability densities of models from sample A and sample B for the major cluster (84.95% population). The cross-correlation of the density maps of the two samples is greater than 0.96.

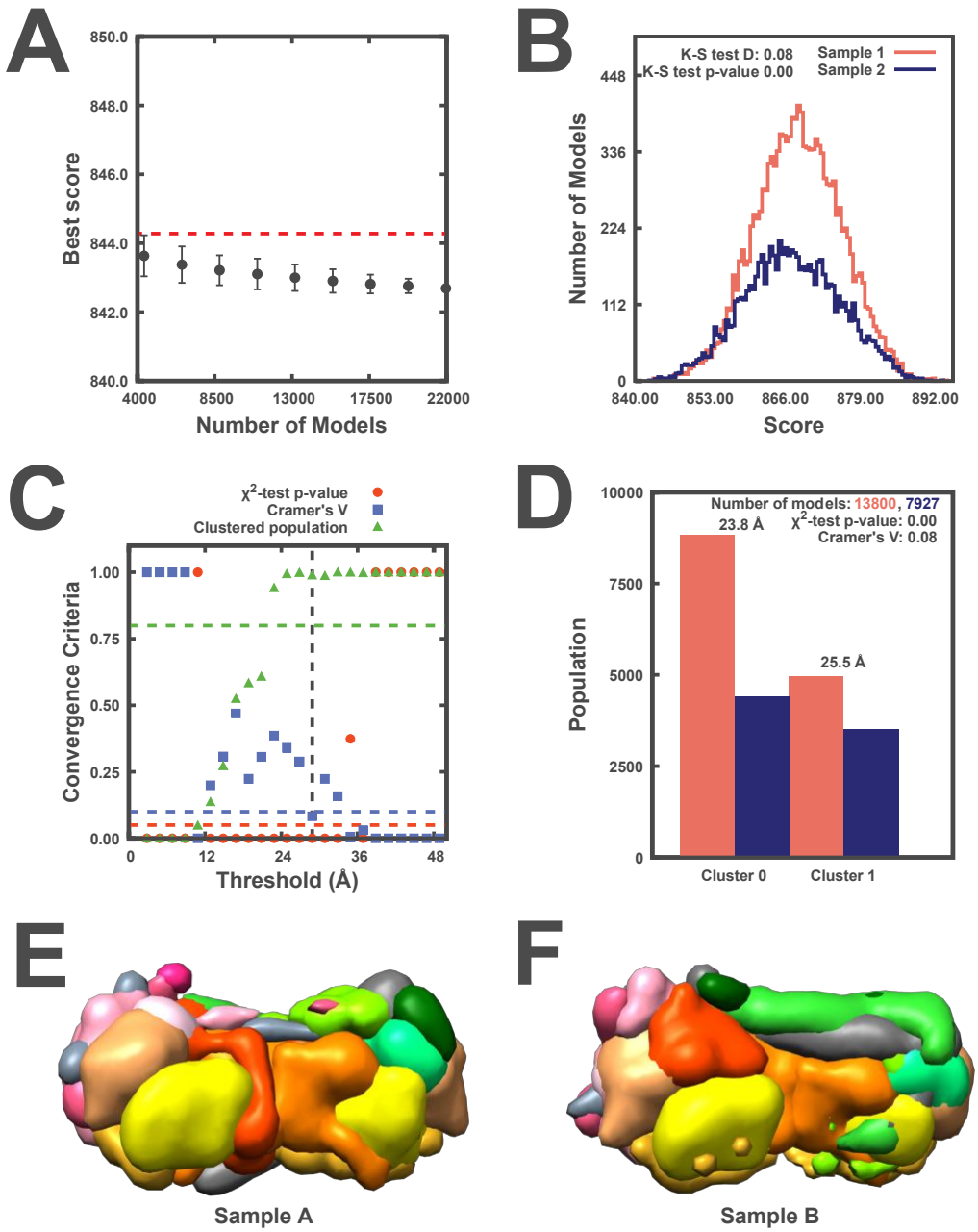

Fig. S4 Sampling exhaustiveness protocol on MTA1^{N}-HDAC1-MBD3^{GATAD2CC} (MHM) models Results of test 1, convergence of the model score, for the 21960 good-scoring models; the scores do not continue to improve as more models are computed essentially independently. The error bar represents the standard deviations of the best scores, estimated by repeating sampling of models 10 times. The red dotted line indicates a lower bound reference on the total score. B. Results of test 2, testing similarity of model score distributions between samples 1 (red) and 2 (blue); the difference in the distribution of scores is significant (Kolmogorov-Smirnov two-sample test p-value less than 0.05) but the magnitude of the difference is small (the Kolmogorov-Smirnov two-sample test statistic D is 0.08); thus, the two score distributions are effectively equal. C. Results of test 3, three criteria for determining the sampling precision (Y-axis), evaluated as a function of the RMSD clustering threshold (X-axis). First, the p-value is computed using the χ^2 -test for homogeneity of proportions (red dots). Second, an effect size for the χ^2-test is quantified by the Cramer's V value (blue squares). Third, the population of models in sufficiently large clusters (containing at least 10 models from each sample) is shown as green triangles. The vertical dotted grey line indicates the RMSD clustering threshold at which three conditions are satisfied (p-value > 0.05 [dotted red line], Cramer's V < 0.10 [dotted blue line], and the population of clustered models > 0.80 [dotted green line]), thus defining the sampling precision of 28.85 Å. D. Populations of sample 1 and 2 models in the clusters obtained by threshold-based clustering using the RMSD threshold of 28.85 Å. Cluster precision is shown for each cluster. E. and F. Results of test 4: comparison of localization probability densities of models from sample A and sample B for the major cluster (60.23% population). The cross-correlation of the density maps of the two samples is greater than 0.95.

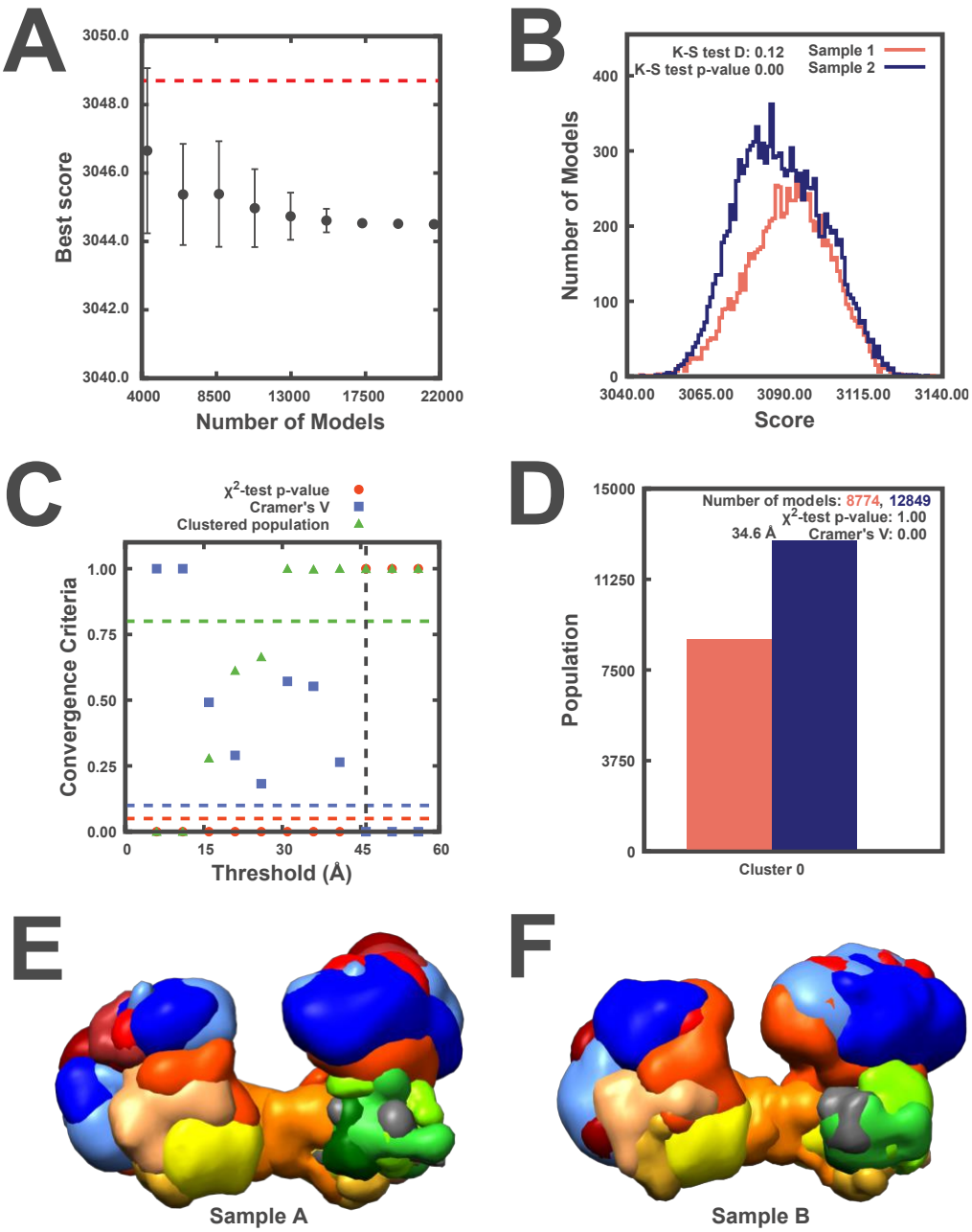

Fig. S5 Sampling exhaustiveness protocol on NuDe integrative models Results of test 1, convergence of the model score, for the 21632 good-scoring models; the scores do not continue to improve as more models are computed essentially independently. The error bar represents the standard deviations of the best scores, estimated by repeating sampling of models 10 times. The red dotted line indicates a lower bound reference on the total score. B. Results of test 2, testing similarity of model score distributions between samples 1 (red) and 2 (blue); the difference in the distribution of scores is significant (Kolmogorov-Smirnov two-sample test p-value less than 0.05) but the magnitude of the difference is small (the Kolmogorov-Smirnov two-sample test statistic D is 0.12); thus, the two score distributions are effectively equal. C. Results of test 3, three criteria for determining the sampling precision (Y-axis), evaluated as a function of the RMSD clustering threshold (X-axis). First, the p-value is computed using the χ^2 -test for homogeneity of proportions (red dots). Second, an effect size for the χ^2-test is quantified by the Cramer's V value (blue squares). Third, the population of models in sufficiently large clusters (containing at least 10 models from each sample) is shown as green triangles. The vertical dotted grey line indicates the RMSD clustering threshold at which three conditions are satisfied (p-value > 0.05 [dotted red line], Cramer's V < 0.10 [dotted blue line], and the population of clustered models > 0.80 [dotted green line]), thus defining the sampling precision of 45.98 Å. D. Populations of sample 1 and 2 models in the clusters obtained by threshold-based clustering using the RMSD threshold of 45.98 Å. Cluster precision is shown for each cluster. E. and F. Results of test 4: comparison of localization probability densities of models from sample A and sample B for the major cluster (99.96% population). The cross-correlation of the density maps of the two samples is ~0.95.

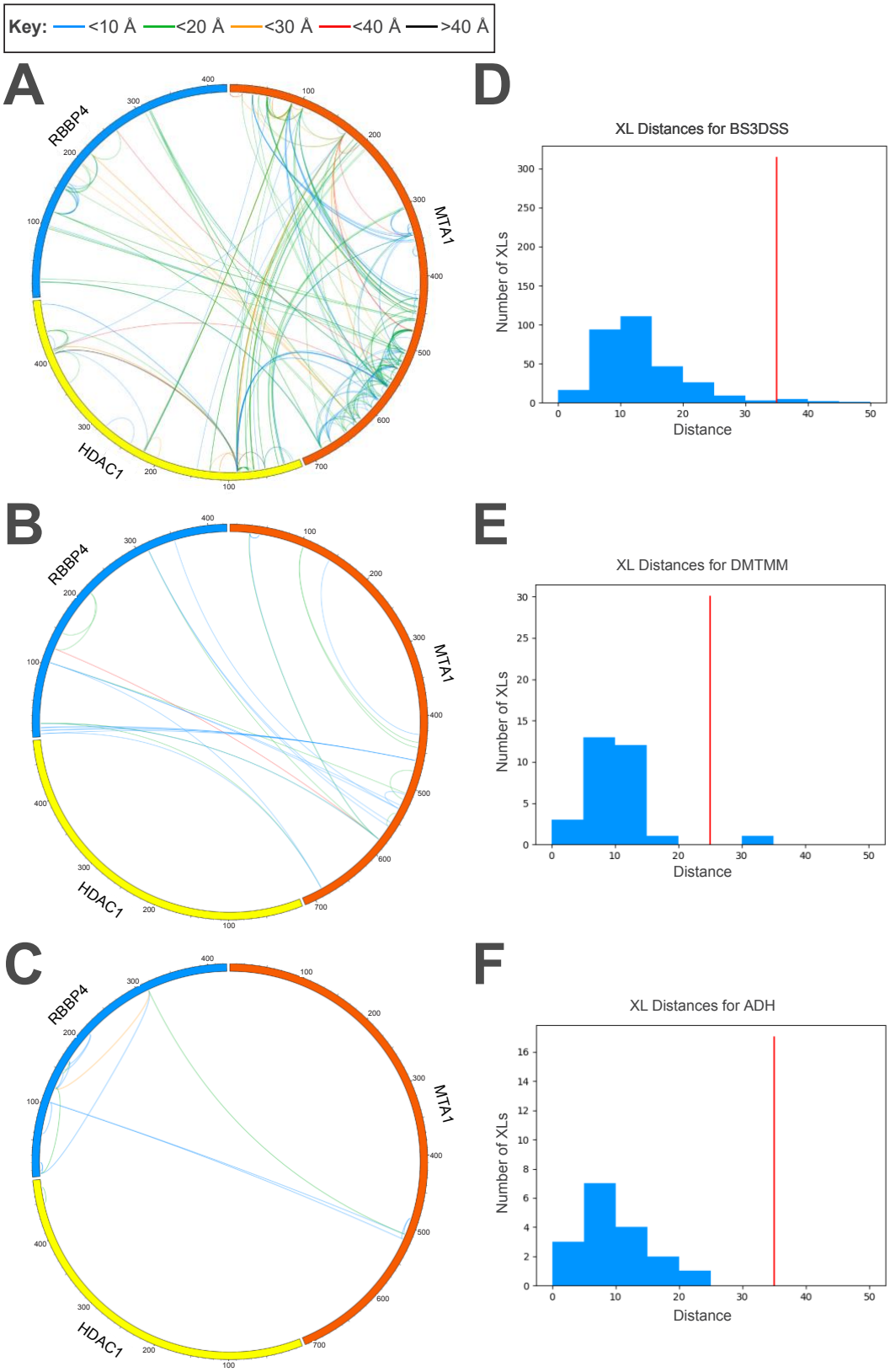

Fig. S6 Results of crosslinks fit for MHR models CX-CIRCOS (http://cx-circos.net/) plots are shown for A. BS3DSS, B. DMTMM, and C. ADH crosslinks on the ensemble of MHR models from the major cluster. Each link depicts a crosslink; its color depicts the minimum distance between the corresponding cross-linked residues in the ensemble, as shown in the color key (top). Histograms showing the distribution of the minimum crosslink distance in the ensemble for D. BS3DSS, E. DMTMM, and F. ADH crosslinks. The red line indicates the distance threshold for a crosslink type.

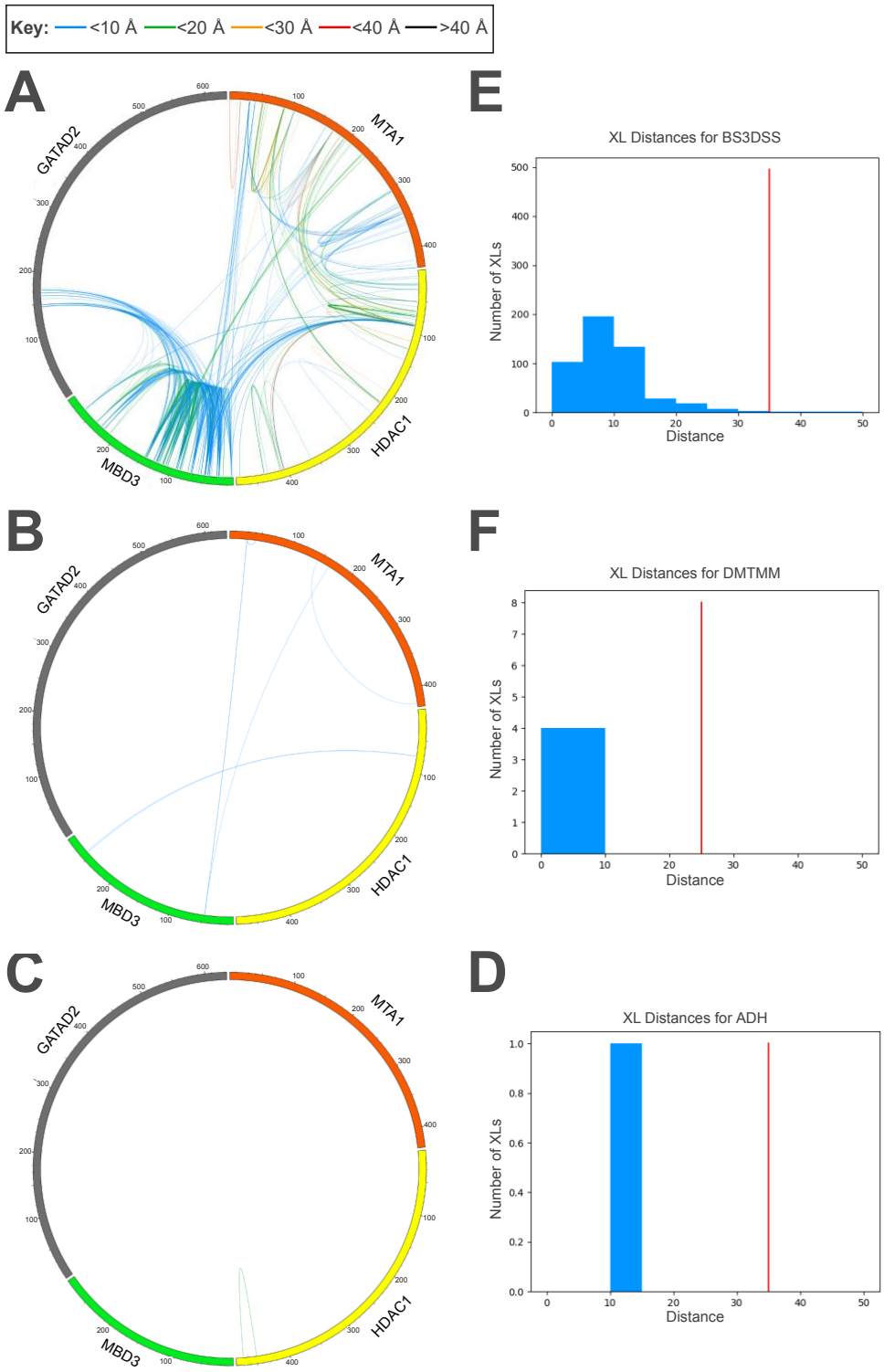

Fig. S7 Results of crosslinks fit for MTA1^{N}-HDAC1-MBD3^{GATAD2CC} (MHM) models CX-CIRCOS (http://cx-circos.net/) plots are shown for A. BS3DSS, B. DMTMM, and C. ADH crosslinks on the ensemble of MHM models from the major cluster. Each link depicts a crosslink; its color depicts the minimum distance between the corresponding cross-linked residues in the ensemble, as shown in the color key (top). Histograms showing the distribution of the minimum crosslink distance in the ensemble for D. BS3DSS, E. DMTMM, and F. ADH crosslinks. The red line indicates the distance threshold for a crosslink type.

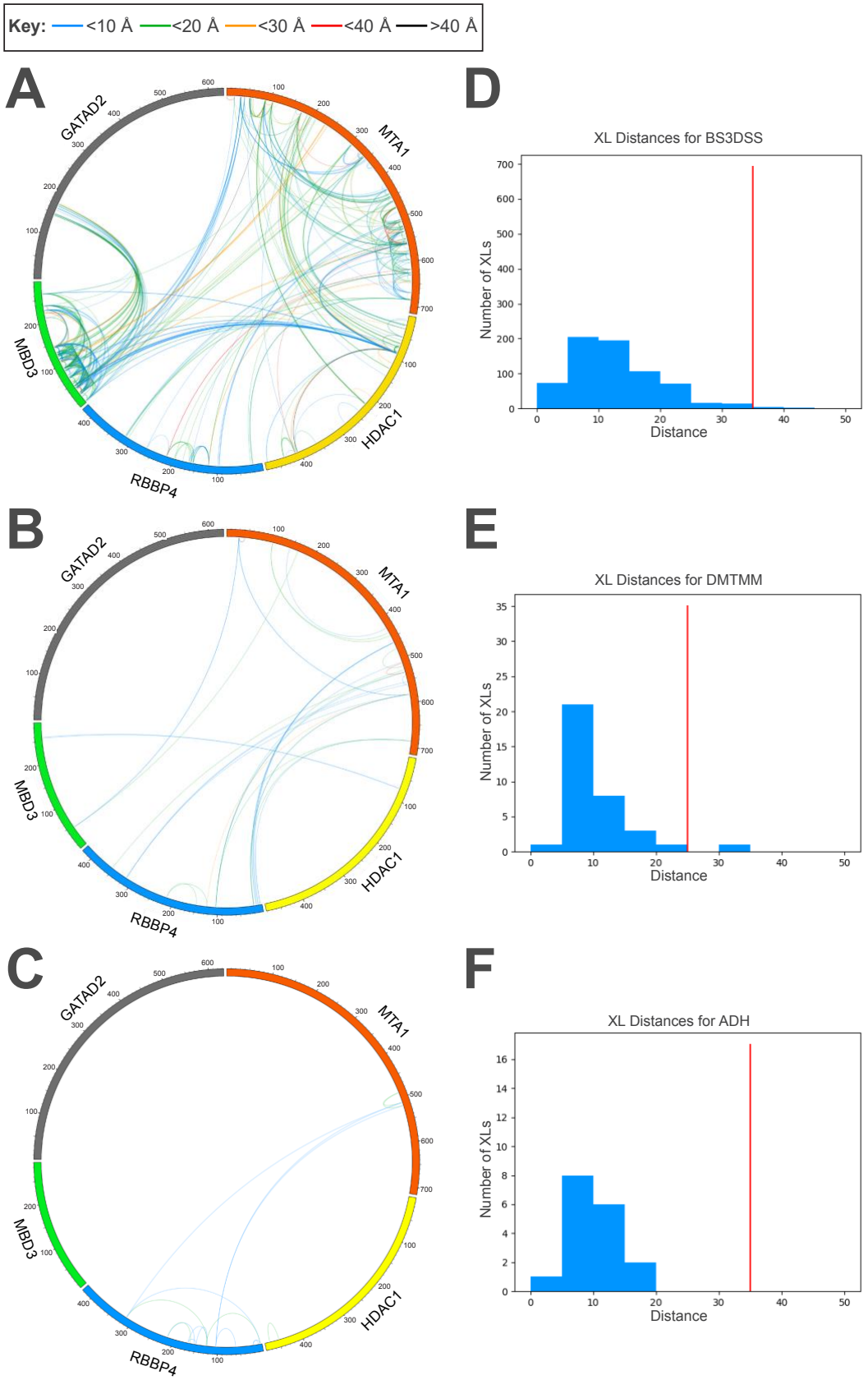

Fig. S8 Results of crosslinks fit for NuDe models CX-CIRCOS (http://cx-circos.net/) plots are shown for A. BS3DSS, B. DMTMM, and C. ADH crosslinks on the ensemble of NuDe models from the major cluster. Each link depicts a crosslink; its color depicts the minimum distance between the corresponding cross-linked residues in the ensemble, as shown in the color key (top). Histograms showing the distribution of the minimum crosslink distance in the ensemble for D. BS3DSS, E. DMTMM, and F. ADH crosslinks. The red line indicates the distance threshold for a crosslink type.

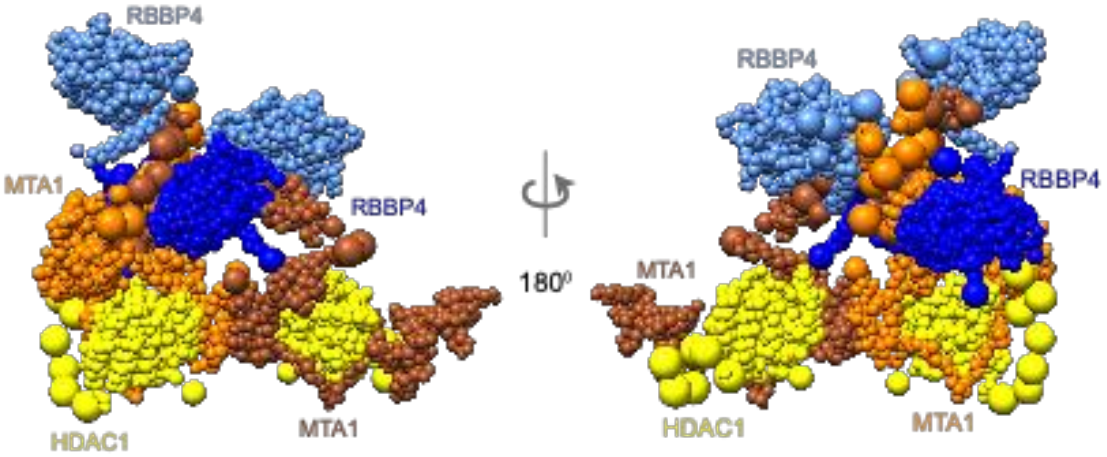

Fig. S9 Integrative model of the MHR complex based on crosslinks alone Representative bead model from the most populated cluster of analyzed integrative models for the MHR complex, colored by subunit. The two copies of MTA1 are shown in different colors (orange and brown) to illustrate the crossover.

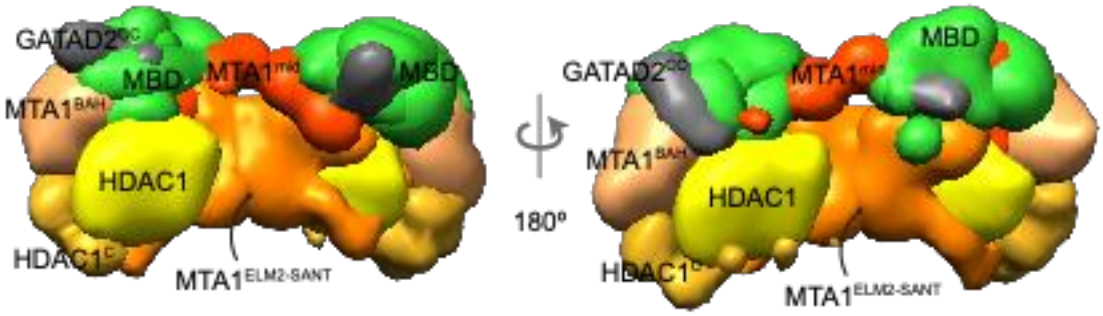

Fig. S10 Integrative model of the MTA1^{N}-HDAC1-MBD3^{GATAD2CC} complex with one copy of MBD3 Localization probability density maps showing the position of different domains in the ensemble of models from the major cluster, illustrating two different binding sites for MBD3 on the MTA1-HDAC1 dimer. The density maps were contoured at 30% (HDAC1 structured region), 5% (HDAC1^{C}, MBD3 and GATAD2^{CC}), 20% (MTA1^{BAH} and MTA1$^{ELM2-SANT}$), and 10% (MTA1^{mid}) of their respective maximum voxel values.

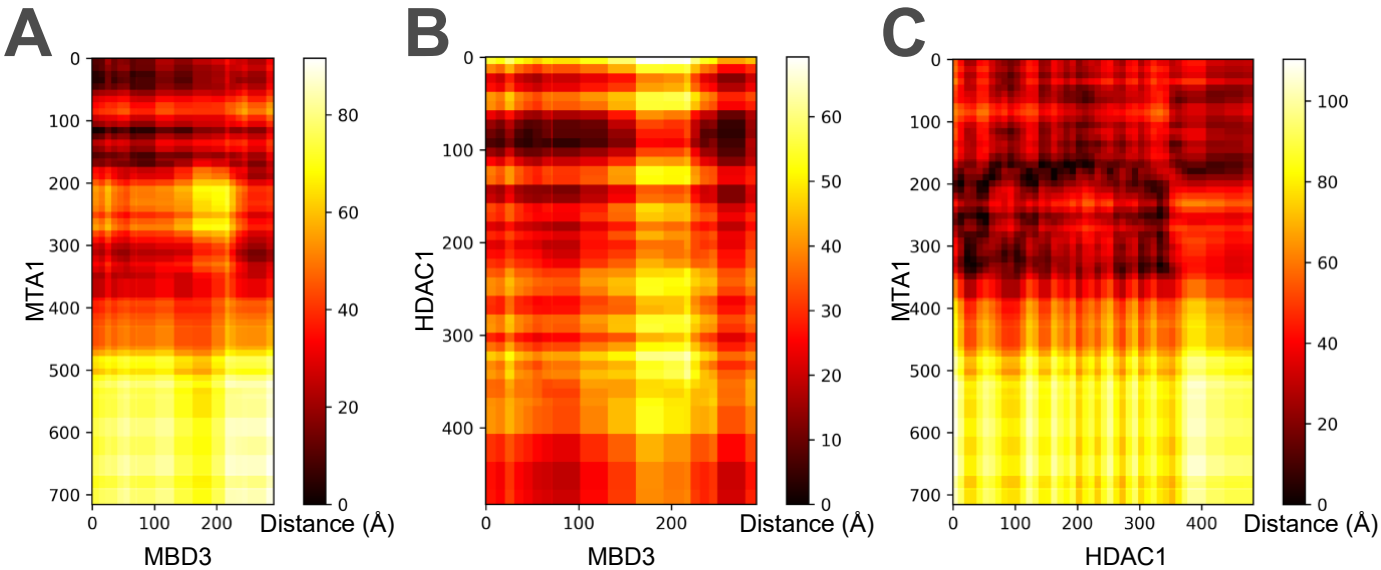

Fig. S11 Distance maps for protein interactions in NuDe. The distance maps show the average pairwise residue distances in the ensemble of NuDe models for the A. MBD3-MTA1, B. MBD3-HDAC1, and C. HDAC1-MTA1 protein pairs. For a pair of residues, the map indicates the distance between the surfaces of the corresponding beads averaged over the ensemble.

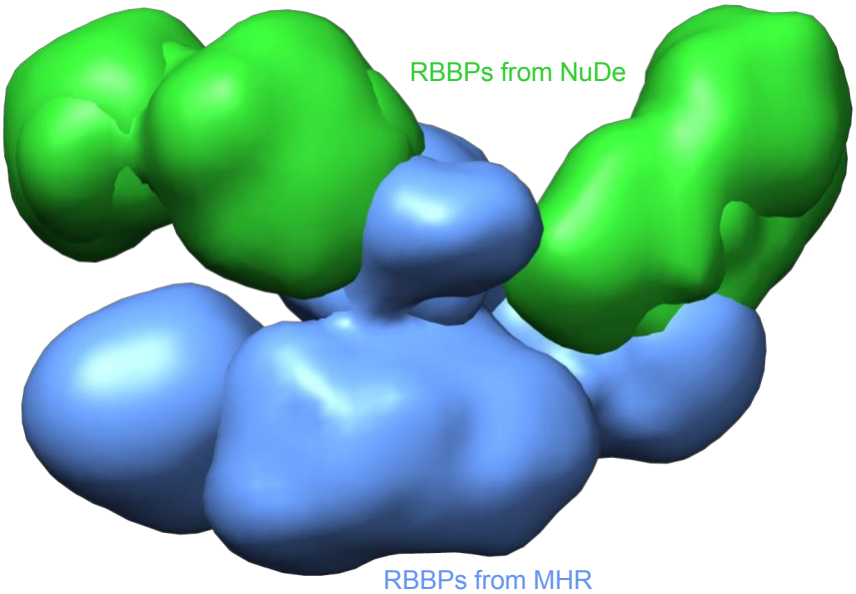

Fig. S12 Densities of RBBPs in MHR and NuDe. The localization probability densities for MTA1^{R1}-RBBP4 and MTA1^{R2}-RBBP4 in MHR (green) and NuDe (blue) are shown. The MHR model shows a broader localization of RBBPs (volume enclosed by the corresponding maps = 1120 nm^3), compared to NuDe (volume enclosed = 883.6 nm^3). All maps were contoured at 10%.

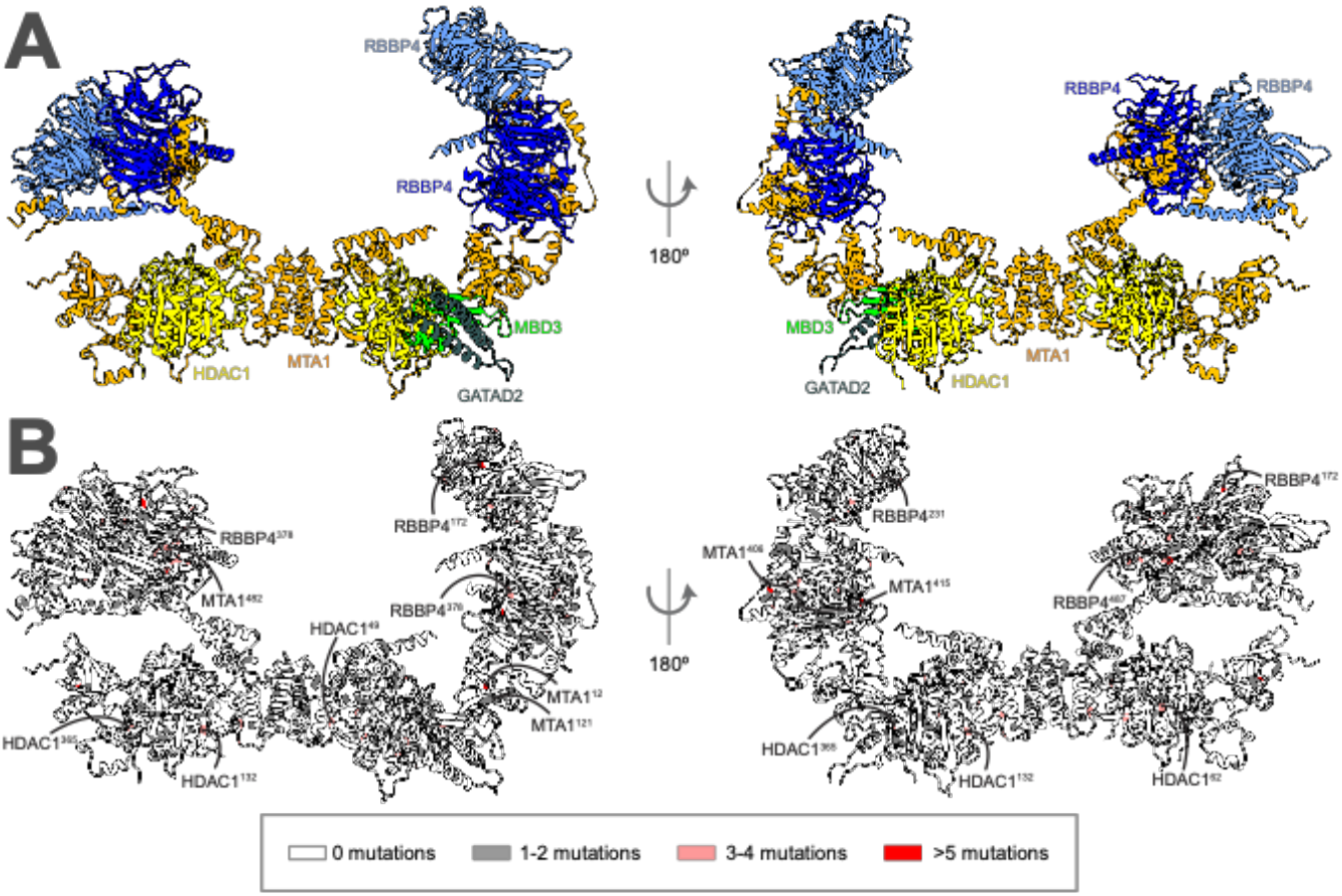

Fig. S13 COSMIC mutations on the structured regions of NuDe complex Somatic, confirmed pathogenic, point mutations from the COSMIC database (Forbes et al., 2006) mapped onto regions with known structure in the NuDe integrative model shown in Fig. 4A. A. Regions with known atomic structure in the integrative model colored by subunit. B. Mutations on residues in regions of known structure, colored according to the legend.

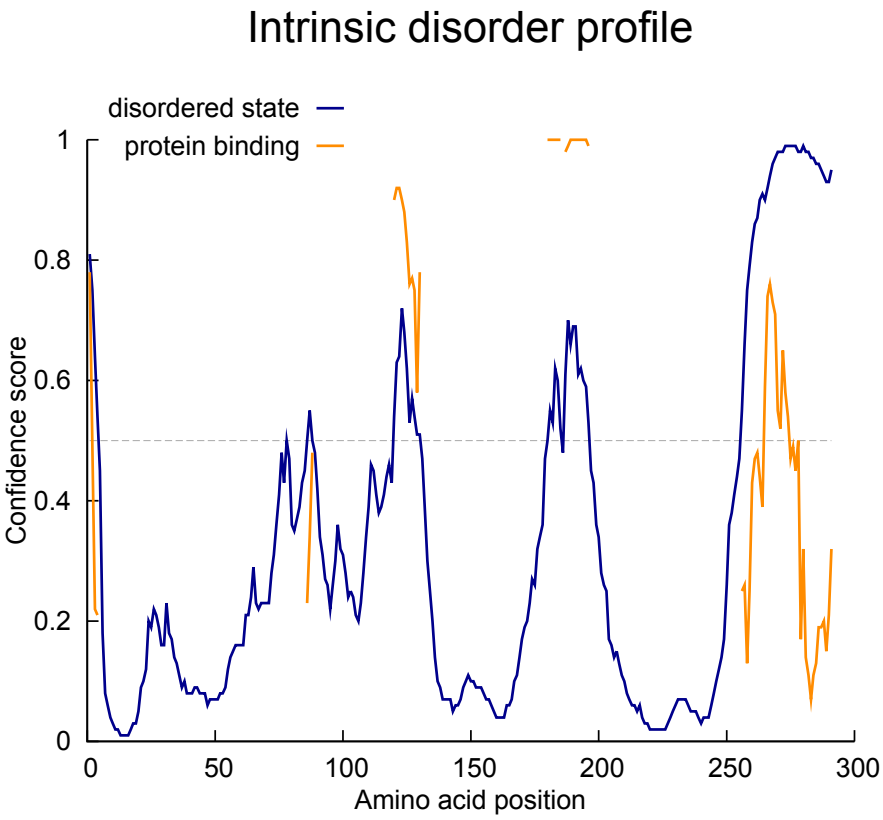

Fig. S14 Disorder prediction for MBD3 PONDR® (http://www.pondr.com) (Romero et al., 2001, 1997) disorder prediction for MBD3.

Table S1. COSMIC Somatic, confirmed pathogenic point mutations from the COSMIC database [(Forbes et al., 2006)] mapped on the NuDe integrative model. A. Mutations in previously undescribed protein-protein interfaces in the model. Residues from two proteins are at an interface if the average distance between their corresponding bead surfaces is less than 10 Å in the cluster of models. B. Mutations in exposed binding sites between modeled proteins and known binding partners, based on the representative NuDe model.

A. COSMIC mutations in previously undescribed protein-protein interfaces in NuDe

NuRD protein	Residues with mutations	Interacting partner in NuRD	Number of COSMIC mutations
MBD3	68, 78, 80, 85, 87, 98, 103, 107, 138, 148, 150, 236, 260, 271, 275	$MTA1^{BAH}$	1-2
$MTA1^{BAH}$	15, 24, 31, 46, 112, 153, 155, 158	MBD3	1-2
	12	MBD3	5+
MBD3	2, 7, 12, 14, 19,31, 39, 41, 43, 45, 55, 65, 68, 78, 80, 85, 87, 98, 103, 107, 111, 125, 130, 138, 148, 150, 236, 240, 243, 250, 260, 271, 275	$HDAC1^{60-100}$	1-2
	17, 60, 112, 128, 246	$HDAC1^{60-100}$	3-4
$HDAC1^{60-100}$	61, 64, 69, 73, 80, 86, 94, 96	MBD3	1-2
	62	MBD3	3-4
$HDAC1^{C}$	411, 420, 423, 425, 431, 435, 447, 462	$MTA1^{BAH}$	1-2
$MTA1^{BAH}$	53, 60, 63, 153, 155, 158	$HDAC1^{C}$	1-2

B. COSMIC mutations in exposed binding sites to known interactors in NuDe

NuRD protein	Residues with mutations	Associated partner outside NuRD if known	Number of COSMIC mutations
RBBP4	39, 45, 71, 75, 128, 321,376, 396, 398	H3, FOG1/2, other ZF containing TFs [(Lejon et al., 2011; Liu et al., 2015; Moody et al., 2018; Schmidberger et al., 2016)]	1-2
RBBP4	40,378	H3, FOG1/2, other ZF containing TFs [(Lejon et al., 2011; Liu et al., 2015; Moody et al., 2018; Schmidberger et al., 2016)]	3-4
$MTA1^{BAH}$	46, 53, 153, 155, 158	Nucleosome (based on Sir3-BAH PDB 3TU4 [6]), MAT1 [(Millard et al., 2014)]	1-2
$MTA1^{mid}$	390, 393, 394, 397, 401, 410, 416, 420, 424	MAT1 [(Mazumdar et al., 2001)]	1-2
$MTA1^{mid}$	406, 415	MAT1 [(Mazumdar et al., 2001)]	3-4
$MTA1^{mid}$	372	NRIF3 [(Talukder et al., 2004)]	5+
$MTA1^{USR}$	547, 550, 562, 564, 578, 581, 601, 603, 606, 610, 611, 612, 617, 619, 633, 646, 647, 652, 658, 666	MICoA [(Mishra et al., 2003)]	1-2
$MTA1^{USR}$	549, 566, 571	MICoA [(Mishra et al., 2003)]	3-4
$MTA1^{C}$	697, 699, 705, 709, 715	MICoA [(Mishra et al., 2003)]	1-2
HDAC1 active site	140, 150, 303	Histone tails, TFs [(Scafuri et al., 2020)]	1-2
$MBD3^{IDR}$	77, 78, 80, 85, 87, 97, 98, 102, 103, 107	Evi1 [(Spensberger & Delwel, 2008)], Aurora A [(Sakai et al., 2002)]	1-2

Movies

M1. MHR movie. The movie shows a sample of one thousand models from the ensemble of MHR integrative models.

M2. MHM movie. The movie shows a sample of one thousand models from the ensemble of MHM integrative models.

M3. NuDe movie. The movie shows a sample of one thousand models from the ensemble of NuDe integrative models.

References:

Armache, K.-J., Garlick, J. D., Canzio, D., Narlikar, G. J., & Kingston, R. E. (2011). Structural Basis of Silencing: Sir3 BAH Domain in Complex with a Nucleosome at 3.0 Å Resolution. *Science*, *334*(6058), 977–982. https://doi.org/10.1126/science.1210915

Forbes, S., Clements, J., Dawson, E., Bamford, S., Webb, T., Dogan, A., Flanagan, A., Teague, J., Wooster, R., Futreal, P. A., & Stratton, M. R. (2006). Cosmic 2005. *British Journal of Cancer*, *94*(2), 318–322. https://doi.org/10.1038/sj.bjc.6602928

Lejon, S., Thong, S. Y., Murthy, A., AlQarni, S., Murzina, N. V., Blobel, G. A., Laue, E. D., & Mackay, J. P. (2011). Insights into Association of the NuRD Complex with FOG-1 from the Crystal Structure of an RbAp48·FOG-1 Complex *. *Journal of Biological Chemistry*, *286*(2), 1196–1203. https://doi.org/10.1074/jbc.M110.195842

Liu, Z., Li, F., Zhang, B., Li, S., Wu, J., & Shi, Y. (2015). Structural Basis of Plant Homeodomain Finger 6 (PHF6) Recognition by the Retinoblastoma Binding Protein 4 (RBBP4) Component of the Nucleosome Remodeling and Deacetylase (NuRD) Complex. *Journal of Biological Chemistry*, *290*(10), 6630–6638. https://doi.org/10.1074/jbc.M114.610196

Mazumdar, A., Wang, R.-A., Mishra, S. K., Adam, L., Bagheri-Yarmand, R., Mandal, M., Vadlamudi, R. K., & Kumar, R. (2001). Transcriptional repression of oestrogen receptor by metastasis-associated protein 1 corepressor. *Nature Cell Biology*, *3*(1), 30–37. https://doi.org/10.1038/35050532

Millard, C. J., Fairall, L., & Schwabe, J. W. R. (2014). Towards an understanding of the structure and function of MTA1. *Cancer and Metastasis Reviews*, *33*(4), 857–867. https://doi.org/10.1007/s10555-014-9513-5

Mishra, S. K., Mazumdar, A., Vadlamudi, R. K., Li, F., Wang, R.-A., Yu, W., Jordan, V. C., Santen, R. J., & Kumar, R. (2003). MICoA, a Novel Metastasis-associated Protein 1 (MTA1) Interacting Protein Coactivator, Regulates Estrogen Receptor-α Transactivation Functions*. *Journal of Biological Chemistry*, *278*(21), 19209–19219. https://doi.org/10.1074/jbc.M301968200

Moody, R. R., Lo, M.-C., Meagher, J. L., Lin, C.-C., Stevers, N. O., Tinsley, S. L., Jung, I., Matvekas, A., Stuckey, J. A., & Sun, D. (2018). Probing the interaction between the histone methyltransferase/deacetylase subunit RBBP4/7 and the transcription factor BCL11A in epigenetic complexes. *The Journal of Biological Chemistry*, *293*(6), 2125–2136. https://doi.org/10.1074/jbc.M117.811463

Punjani, A., Rubinstein, J. L., Fleet, D. J., & Brubaker, M. A. (2017). cryoSPARC: Algorithms for rapid unsupervised cryo-EM structure determination. *Nature Methods*, *14*(3), 290–296. https://doi.org/10.1038/nmeth.4169

Romero, P., Obradovic, Z., Kissinger, C., Villafranca, J. E., & Dunker, A. K. (1997). Identifying disordered regions in proteins from amino acid sequence. *Proceedings of International Conference on Neural Networks (ICNN'97)*, *1*, 90–95 vol.1. https://doi.org/10.1109/ICNN.1997.611643

Romero, P., Obradovic, Z., Li, X., Garner, E. C., Brown, C. J., & Dunker, A. K. (2001). Sequence complexity of disordered protein. *Proteins*, *42*(1), 38–48. https://doi.org/10.1002/1097-0134(20010101)42:1<38::aid-prot50>3.0.co;2-3

Sakai, H., Urano, T., Ookata, K., Kim, M.-H., Hirai, Y., Saito, M., Nojima, Y., & Ishikawa, F. (2002). MBD3 and HDAC1, Two Components of the NuRD Complex, Are Localized at Aurora-A-positive Centrosomes in M Phase *. *Journal of Biological Chemistry*, *277*(50), 48714–48723. https://doi.org/10.1074/jbc.M208461200

Scafuri, B., Bontempo, P., Altucci, L., De Masi, L., & Facchiano, A. (2020). Molecular Docking Simulations on Histone Deacetylases (HDAC)-1 and -2 to Investigate the Flavone Binding. *Biomedicines*, *8*(12). https://doi.org/10.3390/biomedicines8120568

Schmidberger, J. W., Tabar, M. S., Torrado, M., Silva, A. P. G., Landsberg, M. J., Brillault, L., AlQarni, S., Zeng, Y. C., Parker, B. L., Low, J. K. K., & Mackay, J. P. (2016). The MTA1 subunit of the nucleosome remodeling and deacetylase complex can recruit two copies of RBBP4/7. *Protein Science*, *25*(8), 1472–1482. https://doi.org/10.1002/pro.2943

Spensberger, D., & Delwel, R. (2008). A novel interaction between the proto-oncogene Evi1 and histone methyltransferases, SUV39H1 and G9a. *FEBS Letters*, *582*(18), 2761–2767. https://doi.org/10.1016/j.febslet.2008.06.056

Talukder, A. H., Gururaj, A., Mishra, S. K., Vadlamudi, R. K., & Kumar, R. (2004). Metastasis-Associated Protein 1 Interacts with NRIF3, an Estrogen-Inducible Nuclear Receptor Coregulator. *Molecular and Cellular Biology*, *24*(15), 6581–6591. https://doi.org/10.1128/MCB.24.15.6581-6591.2004